UCRL-LR-131742

Numerical Simulation of Fiber and Wire Array Z-pinches with Trac-II

David B. Reisman
(Ph.D Dissertation)

September 1998

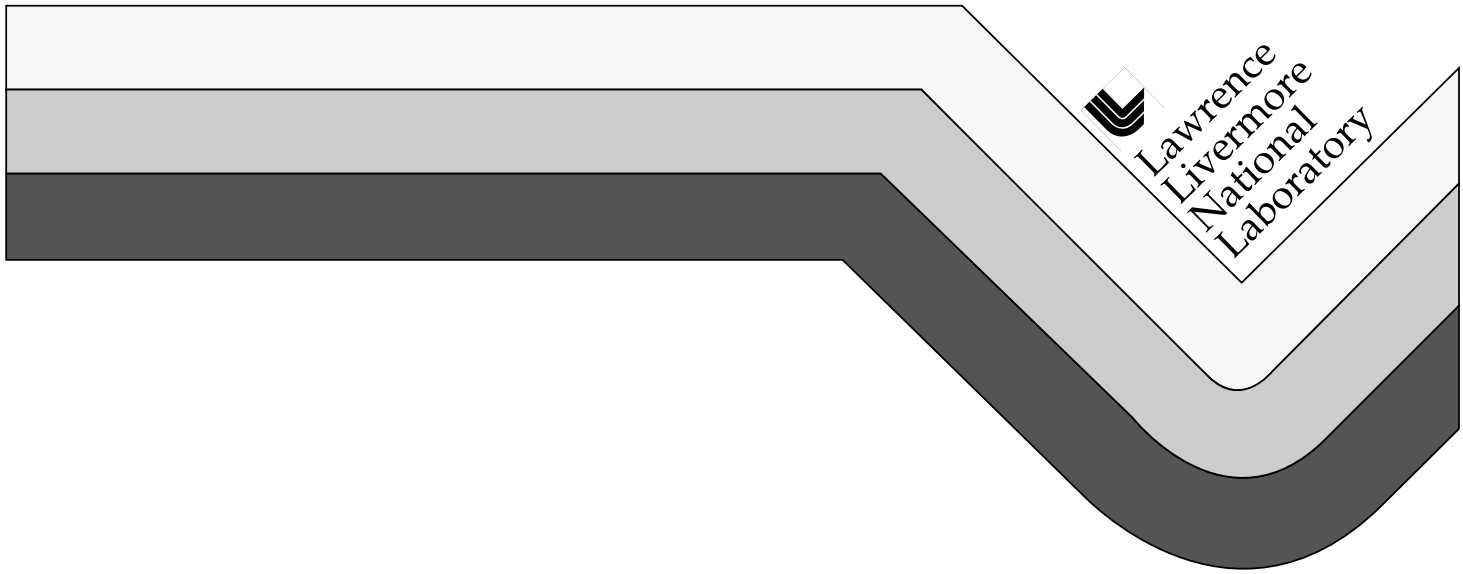

Work performed under the auspices of the U.S. Department of Energy by Lawrence Livermore National Laboratory under Contract W-7405-Eng-48.

UCRL-LR-131742
Distribution Category UC-700

Numerical Simulation of Fiber and Wire Array Z-pinches with Trac-II

David B. Reisman
(Ph.D Dissertation)

September 1998

LAWRENCE LIVERMORE NATIONAL LABORATORY
University of California • Livermore, California • 94551

Numerical Simulation of Fiber and Wire Array Z-pinches with Trac-II

By

DAVID BARTON REISMAN
B.S. (University of California, Davis) 1991
M.S. (Ohio State University) 1993

DISSERTATION

Submitted in partial satisfaction of the requirements for the degree of

DOCTOR OF PHILOSOPHY

in

Physics

in the

OFFICE OF GRADUATE STUDIES

of the

UNIVERSITY OF CALIFORNIA

DAVIS

Approved:

_____

_____

_____

Committee in Charge

1998

David Barton Reisman
September 1998
Physics

Numerical Simulation of Fiber and Wire Array Z-pinches with Trac-II

Abstract

Trac-II is a two dimensional axisymmetric resistive MHD code. It simulates all three spatial components (r, z, ϕ) of the magnetic field and fluid velocity vectors, and the plasma is treated as a single fluid with two temperatures (T_e,T_i). In addition, it can optionally include a self-consistent external circuit. Recent modifications to the code include the addition of the 3-T radiation model, a 4-phase (solid-liquid-vapor-plasma) equation of state model (QEOS), a 4-phase electrical/thermal conductivity model, and an implicit solution of poloidal (B_z,B_r) magnetic field diffusion. These changes permit a detailed study of fiber and wire array Z-pinches. Specifically, Trac-II is used to study the wire array Z-pinch at the PBFA-Z pulse power generator at Sandia National Laboratory. First, in 1-D we examine the behavior of a single wire in the Z-pinch. Then, using these results as initial radial conditions in 2-D, we investigate the dynamics of wire array configurations in the r-z and r-θ plane. In the r-z plane we examine the growth of the m=0 or "sausage" instability in single wires within the array. In the r-θ plane we examine the merging behavior between neighboring wires. Special emphasis is placed on trying to explain how instability growth affects the performance of the Z-pinch. Lastly, we introduce Trac-III, a 3-D MHD code, and illustrate the m=1 or "kink" instability. We also discuss how Trac-III can be modified to simulate the wire array Z-pinch.

Contents

Chapter 1

The Z-pinch

This thesis will mainly be concerned with simulating the early time dynamics of the wire array Z-pinch at the Z accelerator (PBFA-Z) at Sandia National Laboratory (SNL). The Z accelerator is the world's largest X-ray source capable of producing 290 terawatts of power and 1.9 million joules of energy. Recently, there have been dramatic performance increases, measured in X-ray power output, as the result of changing the initial conditions of the wire array. The physical processes behind this result are not well understood. The focus of this thesis is to explain, through numerical simulations, how initial array characteristics ultimately affect the performance of the Z-pinch.

A Z-pinch is created by applying a voltage across a cylindrically symmetric geometry such as a wire, an array of wires, or a cylindrical foil. As the current flows through the wire for instance, the material is heated and ionized, forming a plasma. The current itself produces a strong magnetic field (by Ampere's law) which accelerates the material radially inward (figure 1-1). The plasma column thus pinches on the z-axis producing high densities and temperatures. This energy is then quickly converted to radiation through X-rays. Hydrodynamically speaking, the magnetic field produces a $\overrightarrow{J} \times \overrightarrow{B}$ force which increases the kinetic energy of the fluid. This kinetic energy is converted into electron (and ion) internal energy through pdv work. This electron energy is finally converted into radiation energy which leaves the system as X-rays.

At SNL, the Z accelerator uses a cylindrical array of 100-400 wires of thickness 5-22 μm arranged at a radius of 1-2 cm. The entire array carries a maximum current of 20 million

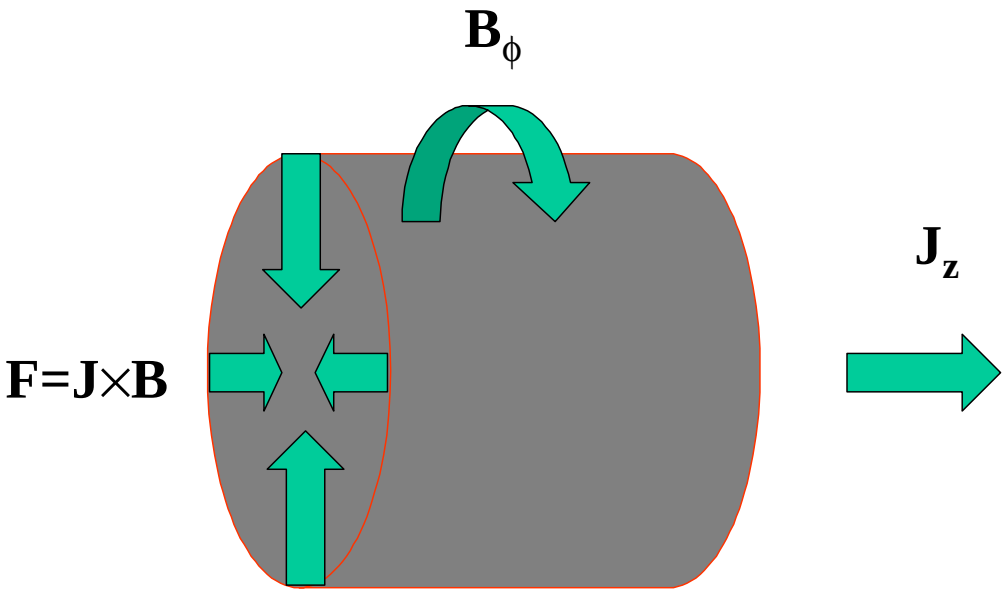

Figure 1-1: Z-Pinch configuration.

amperes during a 100 ns pulse. At peak compression radiation temperatures of 150 eV are reached. Power output is strongly affected by fluid instabilities that occur because of the magnetic pressure applied to the fluid interface. Most notable of these is the Rayleigh-Taylor (RT) instability, a fluid type instability. This will be the subject of some discussion in later chapters.

Dramatic performance increases were first observed on the Saturn machine, a precursor to the Z-accelerator, at SNL. As wire number was increased (and thus interwire gap was decreased) the quality of the implosion and the radiated power was seen to increase monotonically [17]. The same effect was also seen on the Z-accelerator with tungsten wires. As wire number was increased from 120 to 240, the radiated x-ray power increased by (40±20)% [18]. Furthermore, decreasing initial wire diameter on arrays of fixed radius and wire number produced substantial (four-fold) improvements in x-ray performance.

It has been proposed that the performance improvements are attributable to the merging characteristics of the plasma formed when the wires are heated. That is, at some minimum wire spacing (the data from the Saturn experiments suggested that this is 1.4 mm), the wires

are able to form a plasma shell during their initial individual expansion. Subsequently, the array is imploded as a uniform plasma shell with some perturbations that drive RT growth.

1.0.1 Dissertation Problem Statement

The purpose of this thesis is to investigate the individual as well as the merging characteristics of the wire plasma produced in the PBFA-Z experiment. We will attempt to explain why performance increases with either increasing wire number or decreased initial wire diameter. We begin by studying a single wire in the r-z plane. The 1-D calculations show how the wire expands as it is heated and vaporized. 2-D r-z calculations are used to study the growth of the m=0 or "sausage" instability which may be responsible for decreased performance when individual wires repinch in the array. Finally 2D $R-\theta$ calculations are used to study the merging characteristics of the individual wires.

Throughout this thesis we will use Trac-II, a 2-D MHD code, to perform the calculations. Several chapters are devoted entirely to explaining the development of the physics packages added to Trac-II. These were necessary to accurately simulate the Z-pinch system. Appendix A contains a summary of Trac-II as well as the newly incorporated physics models.

Chapter 2

3T Radiation Model

2.1 Derivation of Equation

We begin our derivation with the radiation transfer equation, given in the inertial frame by

$$\frac{1}{c}\frac{\partial I_\nu}{\partial t} + \mathbf{\Omega} \cdot \nabla I_\nu = \eta_\nu - \chi_\nu I_\nu \tag{2.1}$$

where I_ν is the specific intensity, ν is the photon frequency, and $\mathbf{\Omega}$ is the direction angle. The right hand side represents the sum of sources (emission) and sinks (absorption). Our strategy is to first transfer equation 2.1 to the "fluid" or Lagrangian frame $(\nu, \mathbf{\Omega} \rightarrow \nu_o, \mathbf{\Omega o})$ where the photon angles are no longer straight lines and the frequencies are Doppler shifted. Next we integrate over direction angle to obtain moment equations. The angular moments of I_{ν_o} are defined as

$$\begin{aligned} E_o(\nu_o) &= \frac{1}{c}\int I_{\nu_o} d\mathbf{\Omega o} \\ F_o(\nu_o) &= \int I_{\nu_o} \mathbf{\Omega o} d\mathbf{\Omega o} \\ P_o(\nu_o) &= \frac{1}{c}\int I_{\nu_o} \mathbf{\Omega o \Omega o} d\mathbf{\Omega o} \end{aligned} \tag{2.2}$$

Finally we will integrate over all frequencies ν_o to obtain the single group, or "3T", radiation equation.

The derivation of the moment equations is lengthy and can be found in the literature [6][7][8][5]. Our moment equations in cylindrical coordinates (to order $\frac{v}{c}$) are given by the following equations [5].

The 0th moment:

$$\begin{aligned}
&\frac{DE_o}{Dt} + E_o\left[\frac{1}{r}\frac{\partial}{\partial r}(rv_r) + \frac{\partial v_z}{\partial z}\right] + \left[\frac{v_r}{c^2}\frac{\partial F_{or}}{\partial t} + \frac{v_z}{c^2}\frac{\partial F_{oz}}{\partial t} + \frac{1}{r}\frac{\partial}{\partial r}(rF_{or}) + \frac{\partial F_{or}}{\partial z} + \frac{a_r}{c^2}F_{or} + \frac{a_z}{c^2}F_{oz}\right] \\
&-\nu_o\left[\frac{a_r}{c^2}\frac{\partial F_{or}}{\partial \nu_o} + \frac{a_z}{c^2}\frac{\partial F_{oz}}{\partial \nu_o}\right] - \nu_o\left[\frac{\partial v_r}{\partial r}\frac{\partial P_{orr}}{\partial \nu_o} + \frac{v_r}{r}\frac{\partial P_{o\theta\theta}}{\partial \nu_o} + \frac{\partial v_z}{\partial z}\frac{\partial P_{ozz}}{\partial \nu_o} + \frac{\partial v_z}{\partial r}\frac{\partial P_{orz}}{\partial \nu_o} + \frac{\partial v_r}{\partial z}\frac{\partial P_{ozr}}{\partial \nu_o}\right] \\
= \;& 4\pi\eta_o - c\chi_o E_o
\end{aligned} \tag{2.3}$$

The 1st moment in r:

$$\begin{aligned}
&\frac{1}{c}\frac{DF_{or}}{Dt} + \frac{F_{or}}{c}\left[\frac{1}{r}\frac{\partial}{\partial r}(rv_r) + \frac{\partial v_z}{\partial z}\right] + \left[\frac{v_r}{c}\frac{\partial P_{orr}}{\partial t} + \frac{v_z}{c}\frac{\partial P_{orz}}{\partial t} + \frac{a_r}{c}P_{orr} + \frac{a_z}{c}P_{orz}\right] \\
&+c\left[\frac{1}{r}\frac{\partial}{\partial r}(rP_{orr}) + \frac{\partial P_{orz}}{\partial z} - \frac{P_{o\theta\theta}}{r}\right] + \frac{a_r}{c}E_o + \left(\frac{F_{or}}{c}\frac{\partial v_r}{\partial r} + \frac{F_{oz}}{c}\frac{\partial v_r}{\partial z}\right) \\
&-\frac{1}{c}\frac{\partial v_r}{\partial r}\frac{\partial}{\partial \nu_o}(\nu_o Q_{orrr}) - \frac{1}{c}\frac{\partial v_z}{\partial z}\frac{\partial}{\partial \nu_o}(\nu_o Q_{orzz}) - \frac{v_r}{cr}\frac{\partial}{\partial \nu_o}(\nu_o Q_{or\theta\theta}) \\
&-\frac{1}{c}\left(\frac{\partial v_r}{\partial z} + \frac{\partial v_z}{\partial r}\right)\frac{\partial}{\partial \nu_o}(\nu_o Q_{orrz}) - \frac{a_r}{c}\frac{\partial}{\partial \nu_o}(\nu_o P_{orr}) - \frac{a_z}{c}\frac{\partial}{\partial \nu_o}(\nu_o P_{orz}) \\
= \;& -\chi_o F_{or}
\end{aligned} \tag{2.4}$$

The 1st moment in z:

$$\begin{aligned}
&\frac{1}{c}\frac{DF_{oz}}{Dt} + \frac{F_{oz}}{c}\left[\frac{1}{r}\frac{\partial}{\partial r}(rv_r) + \frac{\partial v_z}{\partial z}\right] + \left[\frac{v_r}{c}\frac{\partial P_{ozr}}{\partial t} + \frac{v_z}{c}\frac{\partial P_{ozz}}{\partial t} + \frac{a_r}{c}P_{ozr} + \frac{a_z}{c}P_{ozz}\right] \\
&+c\left[\frac{1}{r}\frac{\partial}{\partial r}(rP_{ozr}) + \frac{\partial P_{ozz}}{\partial z}\right] + \frac{a_z}{c}E_o + \left(\frac{F_{or}}{c}\frac{\partial v_z}{\partial r} + \frac{F_{oz}}{c}\frac{\partial v_z}{\partial z}\right) \\
&-\frac{1}{c}\frac{\partial v_r}{\partial r}\frac{\partial}{\partial \nu_o}(\nu_o Q_{ozrr}) - \frac{1}{c}\frac{\partial v_z}{\partial z}\frac{\partial}{\partial \nu_o}(\nu_o Q_{ozzz}) - \frac{v_r}{cr}\frac{\partial}{\partial \nu_o}(\nu_o Q_{oz\theta\theta}) \\
&-\frac{1}{c}\left(\frac{\partial v_r}{\partial z} + \frac{\partial v_z}{\partial r}\right)\frac{\partial}{\partial \nu_o}(\nu_o Q_{ozrz}) - \frac{a_r}{c}\frac{\partial}{\partial \nu_o}(\nu_o P_{ozr}) - \frac{a_z}{c}\frac{\partial}{\partial \nu_o}(\nu_o P_{ozz}) \\
= \;& -\chi_o F_{oz}
\end{aligned} \tag{2.5}$$

Next we make several approximations. First we take the diffusion approximation and ignore terms of order $\frac{\lambda_p}{\Delta l}\frac{v}{c}$. This term will be of second order since in the diffusion approximation $\lambda_p = \chi_o^{-1}$, the mean free path, will be small compared to our gradient lengths Δl and we are in the nonrelativistic regime ($\frac{v}{c} \ll 1$). We will also drop all acceleration terms. This leaves us with the following 1st moment equations

$$\begin{aligned} -\chi_o F_{or} &= c\frac{1}{r}\frac{\partial}{\partial r}\left(rP_{orr}\right) \\ -\chi_o F_{oz} &= c\frac{\partial}{\partial z}\left(P_{ozz}\right) \end{aligned}$$

Next we assume isotropy (to lowest order in $\frac{\lambda_p}{\Delta l}$):

$$\begin{aligned} P_{orr} &= P_{ozz} = P_{o\theta\theta} = \frac{1}{3}E_o \\ P_{oi\neq j} &= 0 \end{aligned}$$

Now we may write

$$\begin{aligned} F_r &= -\frac{c}{3\chi_o}\frac{1}{r}\frac{\partial}{\partial r}\left(rE_o\right) \\ F_z &= -\frac{c}{3\chi_o}\frac{\partial}{\partial z}\left(E_o\right) \end{aligned}$$

or, more simply

$$\overrightarrow{F_o} = -\frac{c}{3\chi_o}\nabla E_o \tag{2.6}$$

which is "Fick's law" for radiative diffusion.

Turning to our 0th moment equation and again applying the diffusion approximation and isotropy we obtain

$$\begin{aligned} &\frac{DE_o}{Dt} + E_o\left[\frac{1}{r}\frac{\partial}{\partial r}\left(rv_r\right) + \frac{\partial v_z}{\partial z}\right] + \left[\frac{v_r}{c^2}\frac{\partial F_{or}}{\partial t} + \frac{v_z}{c^2}\frac{\partial F_{oz}}{\partial t} + \frac{1}{r}\frac{\partial}{\partial r}\left(rF_{or}\right) + \frac{\partial F_{or}}{\partial z}\right] \\ &-\frac{\nu_o}{3}\left[\frac{\partial v_r}{\partial r} + \frac{v_r}{r} + \frac{\partial v_z}{\partial z}\right]\frac{\partial E_o}{\partial \nu_o} \\ = \;& 4\pi\eta_o - c\chi_o E_o \end{aligned}$$

Or in vector form

$$\frac{DE_o}{Dt} + E_o \nabla \cdot \overrightarrow{v} + \frac{\overrightarrow{v}}{c^2} \cdot \frac{\partial \overrightarrow{F_o}}{\partial t} + \nabla \cdot \overrightarrow{F_o} - \frac{\nu_o}{3} \left(\nabla \cdot \overrightarrow{v} \right) \frac{\partial E_o}{\partial \nu_o} = 4\pi\eta_o - c\chi_o E_o$$

Applying Fick's law we have (the third term drops since it is of order $\frac{\lambda_p}{l}\frac{v}{c}$).

$$\frac{DE_o}{Dt} + E_o \nabla \cdot \overrightarrow{v} - \nabla \cdot \left(\frac{c}{3\chi_o} \nabla E_o \right) - \frac{\nu_o}{3} \left(\nabla \cdot \overrightarrow{v} \right) \frac{\partial E_o}{\partial \nu_o} = 4\pi\eta_o - c\chi_o E_o$$

To obtain our "single group" radiation diffusion equation we integrate over all frequencies ν_o.

$$E = \int_o^\infty d\nu_o E_o \left(\nu_o \right)$$

We obtain

$$\frac{DE}{Dt} + E \nabla \cdot \overrightarrow{v} - \nabla \cdot \overrightarrow{v} \int d\nu_o \left(\frac{\nu_o}{3} \frac{\partial E_o}{\partial \nu_o} \right) - \nabla \cdot \int d\nu_o \left(\frac{c}{3\chi_o} \nabla E_o \right) = \int d\nu_o \left(4\pi\eta_o - c\chi_o E_o \right)$$

We may integrate the third term by parts:

$$\begin{aligned} \int d\nu_o \left(\frac{\nu_o}{3} \frac{\partial E_o}{\partial \nu_o} \right) &= \nu_o E_o \left(\nu_o \right) |_o^\infty - \int d\nu_o \frac{E_o}{3} \\ &= -\frac{E}{3} = P_R \end{aligned}$$

where P_R is the radiation pressure. We write out the total derivative

$$\frac{\partial E}{\partial t} + \overrightarrow{v} \cdot \nabla E + E \nabla \cdot \overrightarrow{v} + P \nabla \cdot \overrightarrow{v} - \nabla \cdot \int d\nu_o \left(\frac{c}{3\chi_o} \nabla E_o \right) = \int d\nu_o \left(4\pi\eta_o - c\chi_o E_o \right)$$

to obtain

$$\frac{\partial E}{\partial t} + \nabla \cdot \left(E \overrightarrow{v} \right) + P_R \nabla \cdot \overrightarrow{v} - \nabla \cdot \int d\nu_o \left(\frac{c}{3\chi_o} \nabla E_o \right) = \int d\nu_o \left(4\pi\eta_o - c\chi_o E_o \right) \qquad (2.7)$$

So far we have said nothing about our actual radiation distribution. If we assume a

Planckian distribution

$$E_o(\nu_o) = \frac{4\pi}{c} B(\nu_o, T_R) = \frac{\hbar}{\pi^2 c^3} \frac{\nu_o^3}{\exp(\hbar\nu_o/T_R) - 1}$$

then our radiation energy density will be

$$E = \int d\nu_o \frac{\hbar}{\pi^2 c^3} \frac{\nu_o^3}{\exp(\hbar\nu_o/T_R) - 1} = aT_R^4$$

where

$$a \equiv \frac{\pi^2}{15(\hbar c)^3}$$

This is Stefan-Boltzmann's law. Furthermore, we may rewrite the right hand of equation 2.7 by assuming LTE - local thermodynamic equilibrium. This assumes a close coupling between matter and radiation and leads to Kirchhoff's law which is given by

$$\eta_o(\nu_o) = \kappa_o(\nu_o) B(\nu_o, T)$$

where T is the matter temperature. If we define the Rosseland mean opacity κ_R (in units of cm^2/g)

$$\begin{aligned} \rho\kappa_R &\equiv \frac{\nabla E}{\int d\nu_o \frac{1}{\chi_o} \nabla E_o(\nu_o)} \\ &= \frac{\frac{\partial B(\nu_o, T_R)}{\partial T_R}}{\int d\nu_o \frac{1}{\chi_o} \frac{\partial B(\nu_o, T_R)}{\partial T_R}} \end{aligned}$$

and the absorption mean opacity

$$\rho\kappa_E = \frac{1}{E} \int d\nu_o \chi_o(\nu_o) E_o(\nu_o)$$

and the Planck mean opacity

$$\rho\kappa_P = \frac{4\pi}{E} \int d\nu_o \kappa_o(\nu_o) B(\nu_o, T)$$

we obtain

$$\frac{\partial}{\partial t}\left(aT_R^4\right) + \nabla \cdot \left(aT_R^4 \overrightarrow{v}\right) + P_R \nabla \cdot \overrightarrow{v} - \nabla \cdot \frac{c}{3\rho\kappa_R} \nabla \left(aT_R^4\right) = ac\rho\left(\kappa_P T^4 - \kappa_E T_R^4\right)$$

Next we make a couple of modifications. First we assume that $\kappa_P \approx \kappa_E$. This will generally be true of optically thick materials. Second, we realize that the flux given by Fick's law can exceed the free-streaming limit, or Stefan's law, if

$$\left|\overrightarrow{F}\right| = -\frac{c}{3\rho\kappa_R}\left|\nabla\left(aT_R^4\right)\right| > \frac{ca}{2}T_R^4$$

or more simply put, if the material becomes "thin" and the Rosseland mean free path exceeds the typical gradients in the problem:

$$\lambda_R = \frac{1}{\rho\kappa_R} \gg \Delta l$$

Therefore, we introduce a "flux limiter" that reproduces the free streaming limit. This is given by

$$\overrightarrow{F}_l = \frac{-\frac{ca}{3}\nabla\left(aT_R^4\right)}{\rho\kappa_R + \frac{2}{3}\frac{\nabla T_R^4}{T_R^4}} \tag{2.8}$$

combining all this into our energy equation we finally obtain

$$\frac{\partial}{\partial t}\left(aT_R^4\right) = -\nabla \cdot \left(aT_R^4 \overrightarrow{v}\right) - P_R \nabla \cdot \overrightarrow{v} - \nabla \cdot \overrightarrow{F_l} + ac\rho\kappa_P\left(T^4 - T_R^4\right) \tag{2.9}$$

The terms on the right represent advection, pdv work, diffusion, and radiation-material coupling, respectively. Note the two physical parameters in the problem - κ_P and κ_R. These are the Planckian and Rosseland means. Usually these will be supplied by tables from the super transition array (STA) model [35][24].

2.2 Numerical Solution

In Trac-II the 3T equation model is "operator split" into diffusion, advection, pdv work, and electron-radiation coupling parts. The advection and pdv work routines are treated

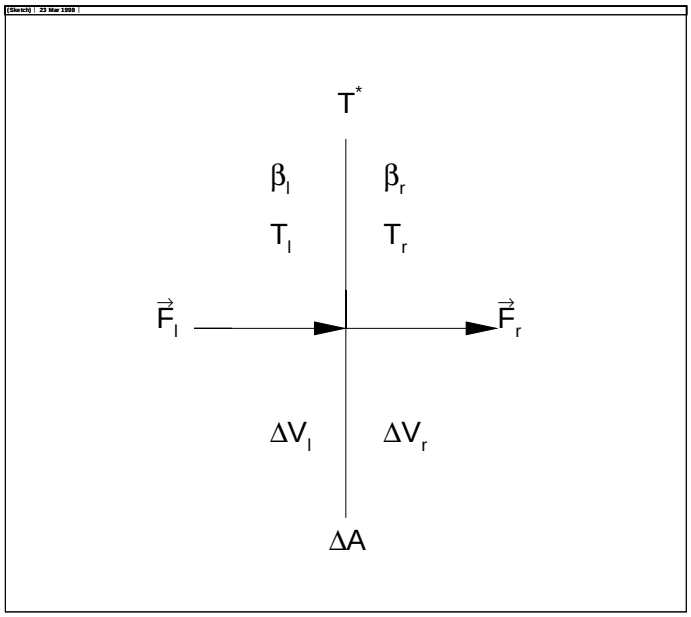

Figure 2-1:

just as their hydro counterparts with radiation pressure and energy replacing electron or ion pressure and energy. The diffusion routine relies on the ICCG (Incomplete Cholesky Conjugate Gradient method) for an implicit solution. The electron-radiation coupling term is solved implicitly as well

2.2.1 Diffusion equation

We must first write the diffusion equation in volume-differenced form. Consistent with Trac-II's numerical scheme, quantities such as density (ρ) and temperature (T) are defined as "zone centered" while diffusion coefficients are defined on the zone faces. To do this we insist that the flux $\overrightarrow{F}$ be continuous across a cell boundary. Consider two adjacent zones, V_r and V_l (figure 2-1).

Here "l" and "r" refer to left and right. We define an average temperature T^* on the face between the two zones. Our equations for right and left hand fluxes are

$$\overrightarrow{F}_l = \beta_l \left(T^{*4} - T_l^4\right) \frac{\triangle A}{\triangle V_l} \tag{2.10}$$

and

$$\overrightarrow{F}_r = \beta_r \left(T_r^4 - T^{*4}\right) \frac{\triangle A}{\triangle V_r} \tag{2.11}$$

by continuity of flux we demand that $\overrightarrow{F}_l = \overrightarrow{F}_r = \overrightarrow{F}$. Solving for T^{*4} we obtain

$$T^{*4} = \frac{\frac{\beta_l}{\triangle V_l} T_l^4 + \frac{\beta r}{\triangle V r} T_r^4}{\frac{\beta_l}{\triangle V_l} + \frac{\beta r}{\triangle V r}} \tag{2.12}$$

substituting this into our equation for $\overrightarrow{F}_l = \overrightarrow{F}_r = \overrightarrow{F}$ we obtain

$$\overrightarrow{F} = \frac{\left(T_r^4 - T_l^4\right) \triangle A}{\frac{\triangle V r}{\beta_r} + \frac{\triangle V_l}{\beta l}} \tag{2.13}$$

But $\beta = \dfrac{ca}{3\rho\kappa_R}$ so we may write

$$\overrightarrow{F} = \frac{ca\left(T_r^4 - T_l^4\right) \triangle A}{3\left(m_r \kappa_{R,r} + m_l \kappa_{R,l}\right)} \tag{2.14}$$

where m refers to the zone mass.

Our diffusion equation can easily be written in volume-differenced form. Integrating over volume and using the divergence theorem

$$\int \frac{\partial (a T_l^4)}{\partial t} dv = \int -\nabla \cdot \overrightarrow{F} dv = -\oint \overrightarrow{F} \cdot d\overrightarrow{A} \tag{2.15}$$

Now consider taking a counterclockwise loop around the faces of a zone labeled "l". All the outside zones will lie to the right ("r") to this zone as shown in figure 2-2. The difference equation is written as

$$-\oint_{zone} \overrightarrow{F} \cdot d\overrightarrow{A} = \sum_r \frac{ca \triangle A_r^2 \left(T_r^4 - T_l^4\right)}{3\left(m_r \kappa_{R,r} + m_l \kappa_{R,l}\right)} = \frac{\triangle (a T_l^4)}{\triangle t} \triangle v_l \tag{2.16}$$

Solving implicitly for T_l^4 we obtain

$$T_l^{(n+1)4} - T_l^{(n)4} = \frac{1}{\triangle v_l} \sum_r f cc_{rl}^{(n)} \left(T_r^{(n+1)4} - T_l^{(n+1)4}\right) \tag{2.17}$$

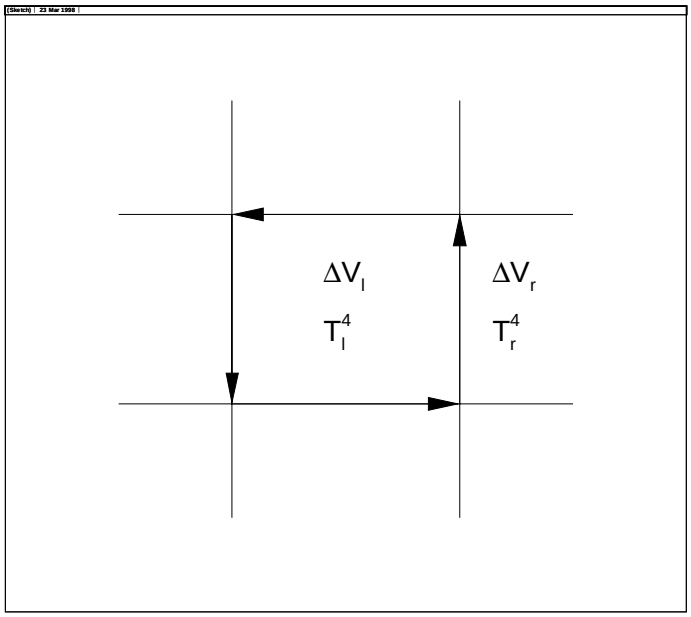

Figure 2-2:

where we may define our "face-centered" diffusion coefficient as

$$fcc_{rl}^{(n)} = \frac{ca\triangle A_r^2}{3\left(m_r\kappa_{R,r} + m_l\kappa_{R,l}\right)} \tag{2.18}$$

Equation 2.18 is really just the familiar 5-point differencing scheme. If we had N zones it would yield a system of N equations which can be re-written in the form of a linear equation: $A \cdot x = y$. Since A is a sparse matrix (only five nonzero elements per row) we must choose an appropriate method. We choose the "conjugate gradient" method - an iterative method - for solving this sparse linear system [9]. Although we will omit the details here, the conjugate gradient method algorithm involves minimizing the equation

$$f(x) = \frac{1}{2}x \cdot A \cdot x - y \cdot x \tag{2.19}$$

which occurs when $\nabla f = A \cdot x - y = 0$. Thus minimizing f is equivalent to solving our linear equation. The minimization is accomplished by iteratively improving x^n with search directions p^n such that $x^{n+1} = x^n + \alpha^n\, p^n$. Here α^n is scalar quantity found at each

iteration which minimizes $f(x^n + \alpha^n p^n)$. The process is continued until a specified tolerance is reached. The "incomplete Cholesky" part of ICCG refers to the "preconditioning" of our linear equation with a specially chosen matrix $\widetilde{A}^{-1}$. With this our linear equation will look like

$$(\widetilde{A}^{-1}A) \cdot x = \widetilde{A}^{-1}y \tag{2.20}$$

If $\widetilde{A}$ is chosen to be close to A then our algorithm will converge in fewer steps as $\widetilde{A}^{-1}A \approx 1$ and $x \approx \widetilde{A}^{-1}y$. In ICCG we will construct $\widetilde{A}^{-1}$ with the Cholesky algorithm, assuming that A and $\widetilde{A}^{-1}$ have the same sparsity structure. That is, $\widetilde{A}^{-1}$ will be a sparse matrix with non-zero elements in exactly the same locations as in A. The ICCG package used in Trac-II uses a slight variant of this method developed at the Center for Applied Scientific Computing at LLNL [25].

2.2.2 Electron-Radiation Coupling

We simultaneously solve the two equations:

$$\frac{\partial(aT_r^4)}{\partial t} = ac\rho\kappa_P \left(T_e^4 - T_r^4\right) \tag{2.21}$$

and

$$c_{ve}\frac{\partial T_e}{\partial t} = -ac\rho\kappa_P \left(T_e^4 - T_r^4\right) \tag{2.22}$$

Problems arise because the second equation has a linear dependence on T_e in the derivative whereas T_e and T_r appear quadratically everywhere else. We will choose to linearize the T_e^4 terms. This is similar to the approach taken in the MACH2 code by Melissa Douglas [16].

Now we rewrite the equations in finite-volume form. First we define several quantities

$$er = \triangle v a T_r^4 \tag{2.23}$$

$$dedte = \triangle v c_{ve} \tag{2.24}$$

$$t_p = (c\rho\kappa_P)^{-1} \tag{2.25}$$

so we may rewrite our equations as

$$\frac{\partial}{\partial t}(er) = t_p^{-1}(a\triangle v T_e^{(n+1)4} - er^{n+1}) \tag{2.26}$$

and

$$dedte\frac{\partial}{\partial t}(T_e) = -t_p^{-1}(a\triangle v T_e^{(n+1)4} - er^{n+1}) \tag{2.27}$$

Note that t_p is the electron-radiation equilibrium time. Next we expand T_e^{n+1} around T_e^n in equation 2.27.

$$dedte\frac{\partial}{\partial t}(T_e) = -t_p^{-1}(a\triangle v T_e^{(n)4} + 4a\triangle v\triangle t T_e^{(n)3}\frac{\partial}{\partial t}(T_e) - er^{n+1})$$

$$dedte\frac{\partial}{\partial t}(T_e) = \frac{-t_p^{-1}}{\left[1 + \dfrac{4a\triangle v\triangle t T_e^{(n)3}}{(dedte)t_p}\right]}(a\triangle v T_e^{(n)4} - er^{n+1}) \tag{2.28}$$

Now impose energy balance and solve for er^{n+1}

$$dedte\frac{\partial}{\partial t}(T_e) = \frac{-t_p^{-1}}{\left[1 + \dfrac{4a\triangle v\triangle t T_e^{(n)3}}{(dedte)t_p}\right]}(a\triangle v T_e^{(n)4} - er^{n+1}) = \frac{\partial}{\partial t}(er) = -\frac{\left(er^{n+1} - er^n\right)}{\triangle t} \tag{2.29}$$

$$er^{n+1} - er^n = \frac{t_p^{-1}\triangle t}{\left[1 + \dfrac{4a\triangle v\triangle t T_e^{(n)3}}{(dedte)t_p}\right]}(a\triangle v T_e^{(n)4} - er^{n+1}) \tag{2.30}$$

define

$$\alpha_{er}^n = \frac{t_p^{-1}\triangle t}{\left[1 + \dfrac{4a\triangle v\triangle t T_e^{(n)3}}{(dedte)t_p}\right]} \tag{2.31}$$

to obtain

$$er^{n+1} = \frac{er^n + \alpha_{er}^n a \triangle v T_e^{(n)4}}{1 + \alpha_{er}^n} \tag{2.32}$$

Now use equation 2.29 to solve for T_e^{n+1}

$$T_e^{n+1} = T_e^n - \frac{\alpha_{er}^n}{dedte}(a \triangle v T_e^{(n)4} - er^{n+1}) \tag{2.33}$$

2.3 Example Problem - Inner Array

As a real-world example of radiatively driven hydrodynamics we consider a "nested" array. This is a configuration consisting of an outer array of tungsten wires arranged at $R_{outer} = 2$ cm with a second inner array of carbon wires positioned at $R_{inner} = 1$ cm. The inner array will consist of 50 60 μm diameter graphite wires. Pinhole images of this type of arrangement [34], but for tungsten wires only, are shown in figure 2-3. The outer array consists of 240 7.1 μm wires at 2 cm and the inner array has 120 8.9 μm wires at 1 cm.

It is believed that the inner array creates a "buffer" onto which the outer array collides and decelerates. Because the growth of the Rayleigh-Taylor instability (a fluid instability dominant effect in wire array Z-pinches) behaves as $e^{\gamma t}$ where $\gamma_{RT} = \sqrt{kg}$, the inner array will have the effect of reducing g. Thus the growth rate γ_{RT} will be reduced. The end effect will be a tighter pinch capable of radiating more efficiently (with a shorter pulse width).

Of some importance is the question of whether the inner array does indeed evaporate and form a buffer. (More work is needed to determine the optimal inner array arrangement for reducing RT growth.). The mechanism for this will be radiative heating from the outer array. As the outer array is imploded, it carries current which produces ohmic heating. This energy is in turn radiated towards the inner array which in turn heats and vaporizes. The problem can crudely be reduced to a 1-D problem of a single graphite wire with a radiation temperature (T_r) boundary condition determined by the radiation temperature of the outer array. This can be provided by another 1-D r-z plane calculation in LASNEX [33]. Of course our problem will end at the time that the outer array collides with the inner array.

The radiation temperature waveform is shown in figure 2-4. We initialize a 1-D carbon

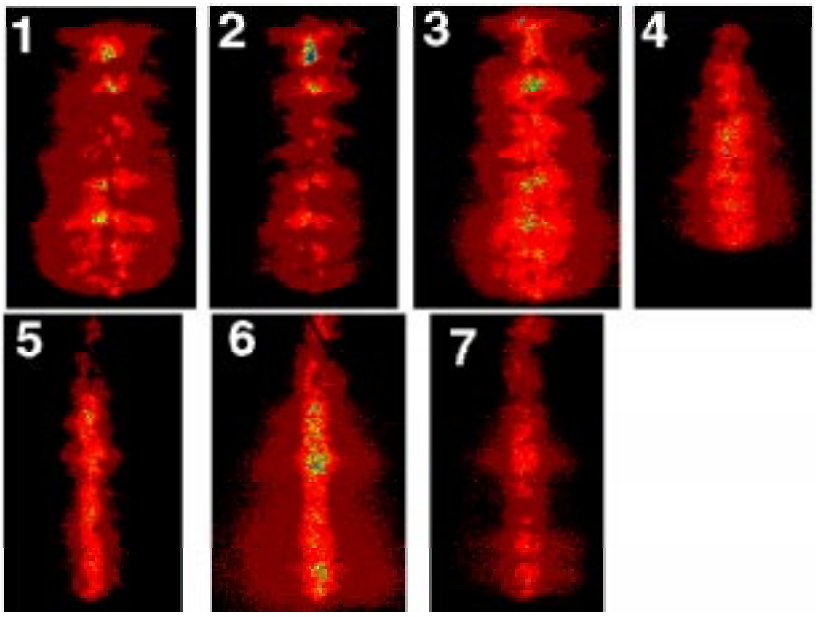

Figure 2-3: Fig. 2. Pinhole images on nested Shot 180 at 1-ns intervals; pinch compression is 40:1.

wire at solid conditions ($\rho = 1.8\ g/cc$, $T_e = T_i = T_r = 2.5 \times 10^{-5}\ KeV$). Later we will describe in more detail how the equation of state is actually modeled. In this case bonding and dense material effects are taken into account. A plot of radii vs. time is shown in figure 2-5.

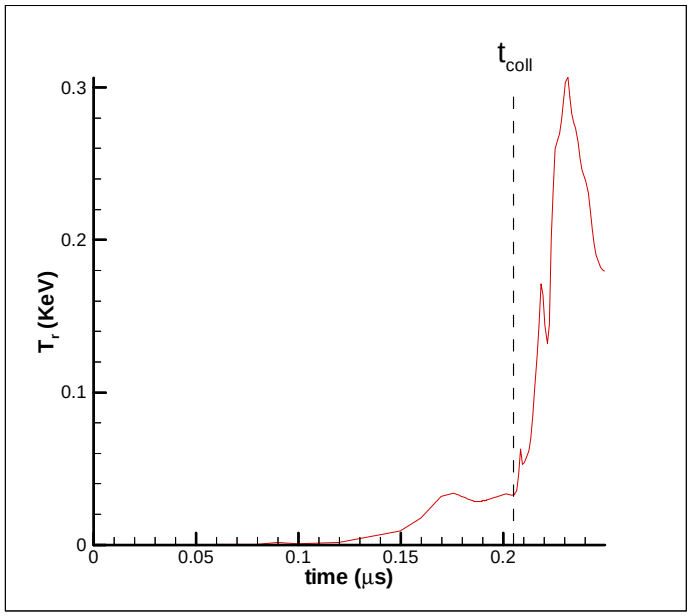

Figure 2-4: Radiation Temperature vs. time. Also shown is t_{coll}, the time that the outer array collides with the inner array.

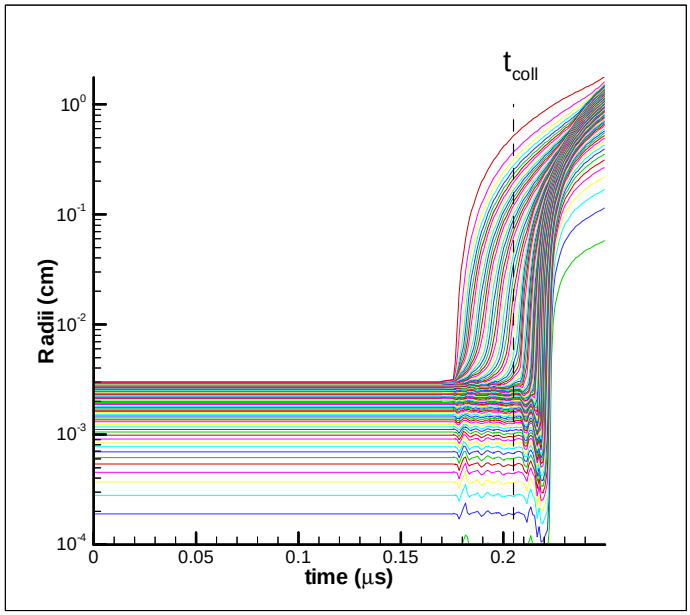

Figure 2-5: Radii vs. time. Grid has 90 zones "feathered" (successively decreased along the r-axis) by a factor of 0.9 .

Chapter 3

Electrical/Thermal Conductivity in Trac-II

3.1 Solid-Liquid Phase

Trac-II uses an analytic model for the electrical conductivity of the solid and liquid phase. It is based on a quantum mechanical model of Mott and Jones [12][22]. Although the details will be omitted here, the model is based on first-order perturbation theory in which τ, the collision time, is calculated. This involves using a perturbed potential, assumed small, which is the difference between the actual potential (with irregularities in the lattice due to thermal vibrations) and the potential of a perfectly regular lattice. The solid conductivity is given by

$$\sigma_s = \sigma_o \left(\frac{T_o}{T}\right)^{\alpha_1} \left(\frac{\rho}{\rho_o}\right)^{2\gamma_o+\alpha_2} \tag{3.1}$$

σ_o is the conductivity at the reference temperature T_o and density ρ_o. α_1 and α_2 are exponents that depend on the specific material. γ_o is the lattice Gruneisen gamma. The liquid conductivity is given simply by

$$\sigma_L = f_m \sigma_s \tag{3.2}$$

f_m is a constant and is .5 for most materials.

We must also be able to choose between the liquid and solid phase. This is accomplished with Lindemann's Law:

$$T_{melt} = \frac{\alpha}{\rho^{2/3}}\Theta_D \tag{3.3}$$

Θ_D, the Debye Temperature, can be calculated through the definition of the Gruneisen gamma. Integrating

$$\gamma = \frac{\partial \ln \Theta_D}{\partial \ln \rho} \tag{3.4}$$

with the assumption that γ has the following density behavior

$$\begin{aligned} \gamma &= \gamma_o - \gamma_a \left(1 - \frac{1}{\eta}\right) \text{ for } \eta \equiv \frac{\rho}{\rho_o} > 1 \\ \gamma &= \gamma_o \text{ for } \eta < 1 \end{aligned} \tag{3.5}$$

we obtain

$$\begin{aligned} T_{melt} &= T_{mo}\eta^{2(\gamma_o - \gamma_a - 1/3)} e^{2\gamma_a(1-1/\ \eta)} \text{ for } \eta > 1 \\ T_{melt} &= T_{mo}\eta^{2(\gamma_o - 1/3)} \text{ for } \eta < 1 \end{aligned} \tag{3.6}$$

where T_{mo} is the melt temperature at the reference density. A plot of the resistivity for tungsten at solid density is shown in figure 3-1

3.2 Vapor Phase Conductivity

At some point, the material will become vaporized. This phase is chosen at the boil temperature and is given simply by

$$T_{boil} = r_b T_{melt} \tag{3.7}$$

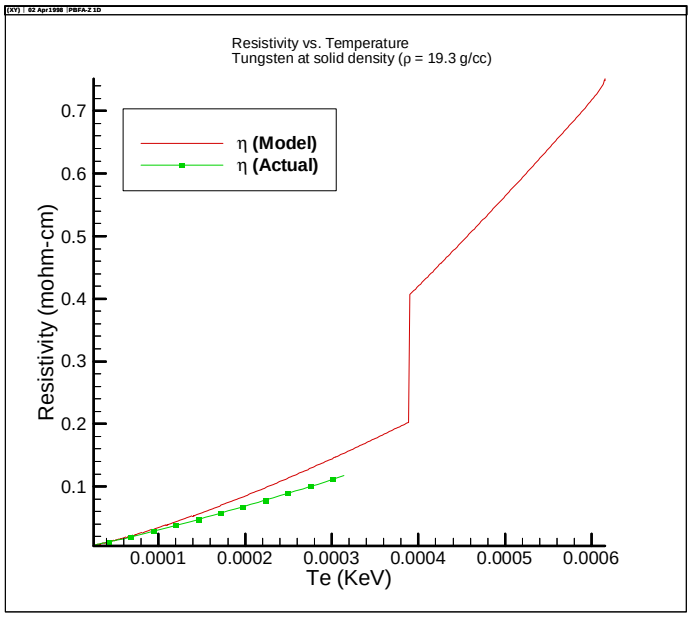

Figure 3-1: Resistivity vs. Temperature for tungsten.

where r_b is a material dependent constant. In this phase only some of the atoms will be ionized. Thus we must consider a resistivity consisting of electron-ion and electron-neutral parts:

$$\eta = \eta_{en} + \eta_{ei} \tag{3.8}$$

where

$$\begin{aligned} \eta_{ei} &= \frac{m\nu_{ei}}{n_e e^2} \\ \eta_{en} &= \frac{m\nu_{en}}{n_e e^2} \end{aligned} \tag{3.9}$$

both these equations can be rewritten in terms of the collision cross section $\nu = n\sigma v$. Thus

$$\eta_{ei} = \frac{m\sigma_i v_{Te}}{Ze^2} \tag{3.10}$$

$$\eta_{en} = \frac{m\sigma_n v_{Te}}{e^2}\left(\frac{n_n}{n_e}\right)$$

For the ion cross section we shall use the interionic spacing

$$\sigma_i = \pi R_o^2 = \pi\left(\frac{3}{4\pi n_i}\right)^{2/3} \tag{3.11}$$

In the vapor phase the plasma condition, given by [3]

$$n_e\lambda_D^3 \sim \frac{T^{3/2}}{n_e^{1/2}} >> 1$$

is no longer satisfied and the Coulomb cross section drops below the minimum cross section given by (3.11). This just expresses the fact that the mean free path cannot be less than the interionic spacing. For the neutral cross section we use the Bohr radius:

$$\sigma_n = \pi R_{Bohr}^2 = 0.88 \times 10^{-16} cm^2 \tag{3.12}$$

The Bohr radius, an estimate of the atomic radius, is a reasonable approximation to the neutral cross section.

Now we need an estimate of the degree of ionization so we may calculate n_e, n_i, and n_n. For that we turn to the Saha equation which assumes chemical equilibrium between these three species. We will also assume, for reasons of convenience, an ideal gas made up of electrons, neutrals and singly ionized atoms (Z=1). The Saha equation for this particular case is [26]

$$\alpha = \left(1 + \frac{n}{2}\frac{g_o}{g_1}\left(\frac{2\pi\hbar}{m}\right)^{3/2}\frac{e^{I_1/T}}{T^{3/2}}\right)^{-1/2} \tag{3.13}$$

where α is the ratio of the number of ionized atoms to the total number of atoms:

$$\alpha \equiv \frac{n_i}{n} \tag{3.14}$$

and I_1 is the ionization potential. g_o and g_1 are the statistical weights, or degeneracy factors, of the atom and ion, respectively. This is determined by the orbital angular momentum

and spin of the ground state:

$$g = (2S+1)(2L+1)$$

Therefore we may calculate our electron-ion and electron-neutral resistivities

$$\begin{aligned} \eta_{ei} &= \frac{m\sigma_i v_{Te}}{e^2} \\ \eta_{en} &= \frac{m\sigma_{Bohr} v_{Te}}{e^2}\left(\alpha^{-1}-1\right) \end{aligned} \tag{3.15}$$

where

$$\sigma_i = \pi\left(\frac{3}{4\pi\alpha n}\right)^{2/3} \tag{3.16}$$

3.3 Thermal Conductivity in the Solid-Liquid-Vapor Phase

For the solid, liquid and vapor phases the thermal conductivity is calculated using the Wiedemann-Franz law which relates thermal conductivity to electrical conductivity [14]:

$$\frac{\kappa}{\sigma} = \frac{\pi^2}{3}\left(\frac{k_B}{e}\right)^2 T \tag{3.17}$$

The derivation of this result involves two assumptions - the relaxation-time approximation and the semiclassical equations of motion. The relaxation-time approximation assumes that electron collisions are effective in maintaining equilibrium and the electron distribution can be described by a local temperature T (the Fermi-Dirac distribution function). The semiclassical equations of motion simply describe the time evolution of the position and wave vector of a electron.

The universal parameter $L = \frac{\pi^2}{3}\left(\frac{k_B}{e}\right)^2 = 2.45\times10^{-8}\left(\frac{volts}{K}\right)^2$ is the Lorentz number. It is found to agree reasonably well with it's experimentally measured value for a large group of metals, including aluminum and tungsten. For instance, aluminum's Lorentz number is $2.19\times10^{-8}\left(\frac{volts}{K}\right)^2$ at 373 K.

3.4 Plasma Phase Conductivity

The plasma conductivity model is based on the work of Lee and More [10]. By solving the linearized Boltzmann equation with a fermionic electron distribution, they obtain an electrical and thermal conductivity in the following form

$$\begin{aligned} \sigma_{\perp} &= \frac{n_e e^2 \tau}{m} A_{\perp}^{\alpha}\left(\mu/k_B T, \omega_e \tau\right) \\ \kappa_{\perp} &= \frac{n_e k_B \left(k_B T\right) \tau}{m} A_{\perp}^{\beta}\left(\mu/k_B T, \omega_e \tau\right) \end{aligned} \tag{3.18}$$

Unlike the familiar Spitzer formula, this conductivity includes degeneracy effects through the dependence on chemical potential. In the non-degenerate limit ($\mu/k_B T - > -\infty$) it reduces to Spitzer's result. Like the Spitzer formula it is dependent on magnetic field through $\omega_e \tau$. This formula is necessary if we are to correctly model hot dense plasmas where Spitzer conductivity may be in error by over a factor of a hundred.

$A_{\perp}^{\alpha}$ and $A_{\perp}^{\beta}$ are given by tabular values. The chemical potential μ is calculated from the Thomas-Fermi model (QEOS) [11] and τ is given by

$$\tau = \frac{3\sqrt{m_e}\left(k_B T\right)^{3/2}}{2\sqrt{2}\pi \left(Z_{eff}\right)^2 n_i e^4 \ln \Lambda} \left[1 + e^{-\mu/K_B T}\right] F_{1/2} \tag{3.19}$$

$F_{1/2}$, a Fermi-Dirac integral, and Z_{eff}, the effective ionization level, are both calculated in the Thomas-Fermi model and are returned from QEOS subroutines. The plasma conductivity given above is chosen when it exceeds the vapor conductivity. That is,

$$\sigma = \max\left(\sigma_{plasma}, \sigma_{vapor}\right)$$

3.5 A Note About Parameters

For tungsten and aluminum the following constants are used in equations 3.1-3.6 [22]

Constant	W	Al
σ_o	178.57 (mohm-cm)$^{-1}$	354.11 (mohm-cm)$^{-1}$
T_o	0.0256916 eV	0.025 eV
ρ_o	19.3 g/cc	2.703 g/cc
α_1	1.3192	1.1433
α_2	1.	-1.
γ_o	1.67	1.93
γ_a	1.3	1.5
f_m	0.5	0.5
r_b	1.6109	1.6720
T_{mo}	0.39 eV	0.20508 eV

The Ionization potentials and degeneracy factors used in equation (3.13) [15] are:

Constant	W	Al
I_1	7.98 eV	5.986 eV
g_o	1	6
g_1	2	1

Chapter 4

Trac-II Equation of State - QEOS

4.1 Thomas-Fermi and Cowan Ion Model

Trac-II uses the Quotidian Equation of State (QEOS) [11] to calculate electron and ion pressure and energy for use in the hydrodynamic routines. QEOS also enters in various diffusion routines through its calculation of the ionization level Z_{eff} and the electron-ion collision time τ. QEOS is a self consistent analytic model which is valid over a large range of densities and temperatures. For our uses, it will allow us to model the behavior of tungsten wire through all four phases.

QEOS uses separate electron and ion temperatures and assumes electron and ion quantities are additive. For the electron part, QEOS uses the Thomas-Fermi model [26][27]. This model assumes each ion is surrounded by a sphere of charge satisfying the usual Fermi-Dirac statistics. The radius of the charge sphere is $R_o = \left(\frac{3}{4\pi n_i}\right)^{1/3}$. Thus the charge state is found to be

$$Z_{eff} = \frac{4\pi}{3} R_o^3 n\left(R_o\right) \tag{4.1}$$

Thermodynamic functions such as energy, free energy and entropy (given by the formulae for a finite temperature semiclassical gas) are calculated with the self-consistent solution of Poison's equation for the electrostatic potential $V(r)$:

$$\nabla^2 V(r) = 4\pi e n(r) - 4\pi Z e \delta(r) \tag{4.2}$$

Of course, once the thermodynamic functions are determined, thermodynamic quantities such as pressure and energy may be calculated through functional derivatives. In practice, QEOS uses tabular values for the free energy to evaluate thermodynamic values.

For the ion part of the equation of state, QEOS uses the Cowan ion model. This analytic model incorporates several well known laws in their appropriate limits to obtain an equation of state valid for a large range of temperatures and densities. For instance, the Dulong-Petit law, the Gruneisen pressure law, and the ideal gas law are included in the Cowan ion model. Like the Thomas-Fermi part of QEOS, a free energy is calculated from which thermodynamic quantities can be obtained.

4.2 Bonding Model

Due to the Pauli Exclusion Principle, the Thomas-Fermi model will predict positive pressures at solid conditions. To compensate for this, QEOS uses a semi-empirical bonding model that introduces an additive correction to the energy and pressure:

$$\begin{aligned} E_b &= E_o(1 - \exp b\left[1 - \left(\frac{\rho_s}{\rho}\right)^{1/3}\right]) \\ p_b &= \rho^2 \frac{\partial E_b}{\partial \rho} = -\left(\frac{E_o b \rho_s}{3}\right)\left(\frac{\rho}{\rho_s}\right)^{2/3} \exp b\left[1 - \left(\frac{\rho_s}{\rho}\right)^{1/3}\right] \end{aligned} \tag{4.3}$$

The constants E_o and b are determined from the requirement that the total solid pressure equal zero ($p_{TOT}(\rho_s, T=0) = 0$ where $p_{TOT} = p_e + p_i + p_b$) and the calculated bulk modulus equal its experimental value ($\mathrm{B_{exp}} = \rho\left(\frac{\partial p_{TOT}}{\partial \rho}\right)$). Unfortunately, using this procedure, QEOS will predict a melting temperature of about 1.5 eV for all materials. In practice, the experimental bulk modulus, an input quantity, must be slightly adjusted to give the correct melting point. In any event, this bonding correction will have little effect away from the solid region.

4.3 Implementation of QEOS in Trac-II

Trac-II uses the following QEOS "vectorized" subroutines [11] in which density and temperature are input quantities

$$eostfv\,(i1, i2, inc, t, rho, z, a, z23, p, dpdt, dpdrho, e, dedt, s, zeff) \tag{4.4}$$
$$eosiv\,(i1, i2, inc, t, rho, z, a, p, dpdt, dpdrho, e, dedt, s)$$
$$chemp\,(vi1, i2, inc, t, rho, zeff, a, xmu)$$

These are the Thomas-Fermi, Cowan-Ion, and chemical potential subroutines, respectively. Also used is the bonding correction subroutine which requires various bonding parameters such as uncorrected pressure and energy, solid density, and the difference between uncorrected and corrected bulk modulus:

$$bondcorv\,(i1, i2, inc, rho, rho0, p0, e0, dbm, p, dpdrho, e) \tag{4.5}$$

After the plasma is initialized, electron and ion energies are treated as fundamental variables and are not altered by QEOS. When an energy is incremented, say in the hydro routines, QEOS specific heats are used to increment electron and ion temperatures. Finally, the temperatures are adjusted at each timestep to be consistent with their energies through a single Newton-Raphson step.

4.4 Example Problem: Current Posts in PBFA-Z

To illustrate the use of QEOS and the 4-phase conductivity model we consider the flow of current through a stainless steel post. Our intention here is to model the effects of large currents on the PBFA-Z apparatus (PBFA-Z and the Z-pinch will be discussed in greater detail in the next chapter.). At issue here is the amount of current that can be carried by a post. At high current densities ($\frac{I}{2\pi R_{post}} \sim 10\ MA/cm$) shocks and ohmic losses become important. We consider two different diameter posts - 0.3 and 6.0 cm - and use an equivalent circuit (L,R,V(t)) from the actual experiment.

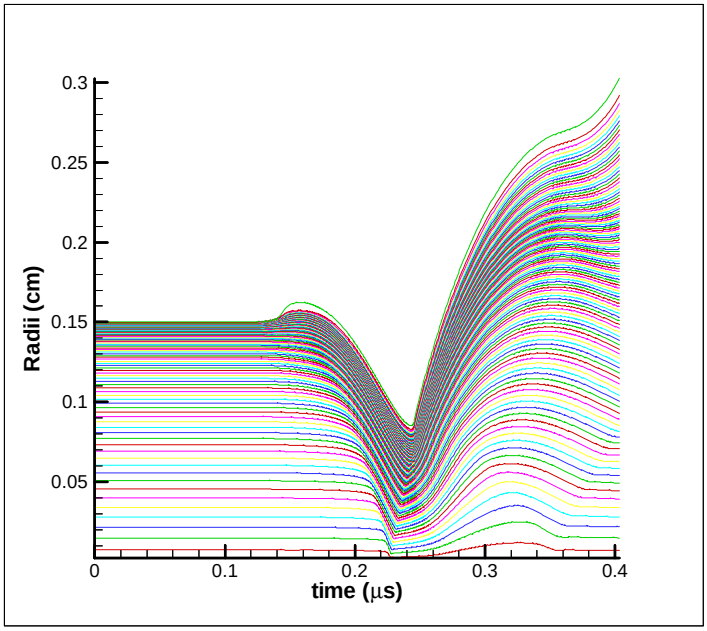

Figure 4-1: Radii vs. time for 0.3 cm diameter post.

The 6.0 cm post will remain solid during the entire current pulse. However, the 0.3 cm post will undergo several phase changes as it is ohmically heated and then compressed by the large magnetic pressure generated by the current. A plot of radii vs. time for the 0.3 cm post case is shown in figure 4-1. We see that the large magnetic pressures produce a strong shock in the post.

These results have been compared to other rad-hydro calculations and shown to agree within 10% [19]. Later this summer (8/98), high current density energy loss experiments will be performed at the Z facility. These experimental results will be compared to these predictions and future 2-D calculations using Trac-II. Of primary importance is the energy loss expected in X-1, the planned next-generation Z-pinch accelerator, which will be capable of a peak current of 60 MA.

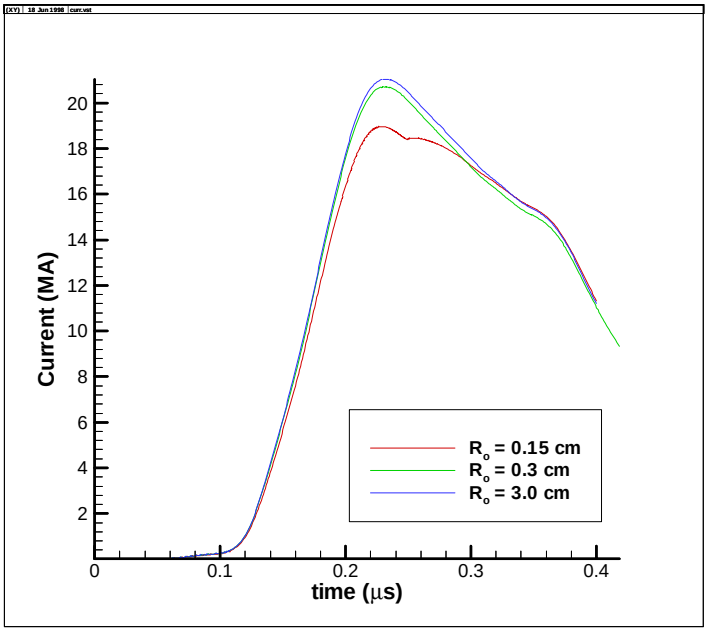

Figure 4-2: Circuit current for various post diameters.

Chapter 5

The Z-pinch: 1-D results for a single wire

5.1 PBFA-Z Prepulse

We first use the improvements in Trac-II to study the initiation of a single wire in the PBFA-Z wire array at Sandia National Laboratory. The voltage applied to the wire is determined from the actual PBFA-Z voltage waveform (figure 5-1). A self consistent LR circuit model is solved at each timestep using the equivalent inductance and resistance from the experiment. Of course L and R for this single wire must be scaled appropriately:

$$\begin{aligned} L_{wire} &= N L_{array} \\ R_{wire} &= N R_{array} \end{aligned} \tag{5.1}$$

where N is the number of wires in the array. The code will then calculate $rB_\phi = 2I_{enc}$ at the boundary which will drive the dynamics of the problem.

Specifically we consider a 10 μm diameter tungsten wire from a PBFAZ shot of 180 wires. The length of wires in the array is 2 cm and the array diameter is 3 cm. We will

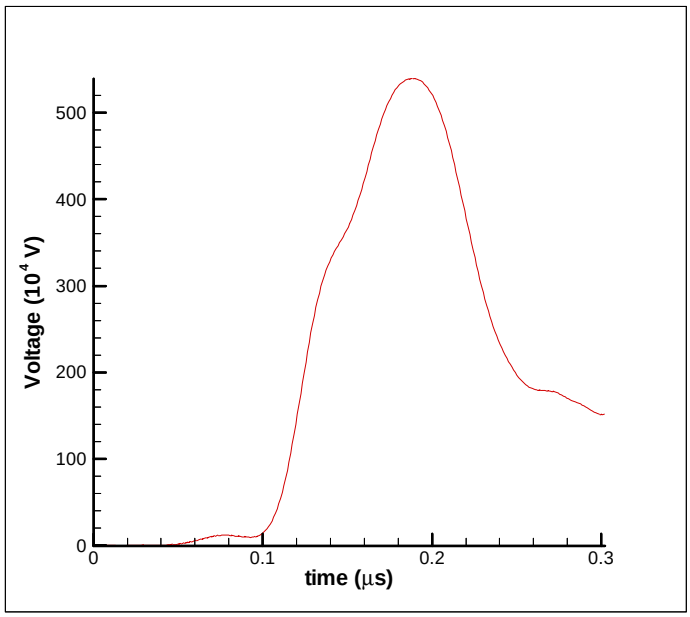

Figure 5-1: PBFA-Z equivalent voltage.

begin with a solid tungsten wire at room temperature:

$$\begin{aligned} T_e &= T_i = T_r = 2.5 \times 10^{-5} KeV \\ \rho &= 19.3\ g/cc \end{aligned} \tag{5.2}$$

For this calculation we implicitly solve electron and ion thermal diffusion. The magnetic field, B_ϕ, is solved implicitly as well. As mentioned before, we will use the 3-T radiation diffusion with opacities from the STA atomic physics model [24]. Our mesh will be pure Lagrangian with 72 zones in the radial direction. The zones must be "feathered" (decreased geometrically in the r-direction) to resolve current flowing in the corona of the plasma properly. Our feathering factor will be 0.9 and our outermost zone will have a thickness of only 3Å.

5.2 Results

The wire remains solid for the first 0.06 μs of the problem. The initial resistivity is so high that current flows uniformly through the wire which is in turn heated uniformly. When the vapor temperature is reached (This is approximately .6 eV for tungsten) , the wire expands and develops a "skin" where most of the current flows. During this initial expansion phase between 0.06-0.12 μs very little of the wire is converted into plasma. As a rough measure we define the fraction of the wire mass that has density below one-hundreth of solid density ($\rho < 0.193$). This we define as the "involved mass". We find that only 2-10% of the wire has a density below this level. In fact, the outer zones have a density of around $10^{-5} - 10^{-6}$ g/cc and are expanding at a rate of approximately 1-3 $cm/\mu s$. At this stage our wire remains in a liquid-solid phase with a low-density plasma corona.

At about 120 ns into the problem magnetic pressure is sufficient to repinch the low-density corona. The density of the outer corona will increase by more that an order of magnitude during this first pinch phase (0.12-0.14 μs). Therefore, the electron-radiation coupling will increase sharply as $ac\rho\kappa_P \sim \rho^2$. The electron and radiation temperatures will come into equilibrium in the corona due to this large increase in coupling and a radiation wave will be sent through the entire wire. This is most clearly seen in figure 5-5 where the radiation and electron temperature in the innermost zone are plotted as a function of time. Before the repinch the plasma temperature oscillates around the vapor temperature. Then, the radiation temperature of the zone rises and thus drives up the material temperature past the vapor point. Between 0.15-0.16 μs both temperatures rise dramatically as the region expands.

The wire is completely vaporized after this first pinch. Furthermore, radiation losses also become significant when compared with total energy (figure 5-6). Subsequent repinches release large amounts of energy through radiation. However, by the time of peak current (0.2 μs), the entire array has begun to implode towards the axis and a single wire calculation is not particularly meaningful. Furthermore, the single wire calculations are clearly only valid until the plasma formed from individual wires crosses the the initial gap between the wires. In this particular case we see that the radial expansion exceeds half the gap distance (figure 5-2). This will be discussed further in chapter 6.

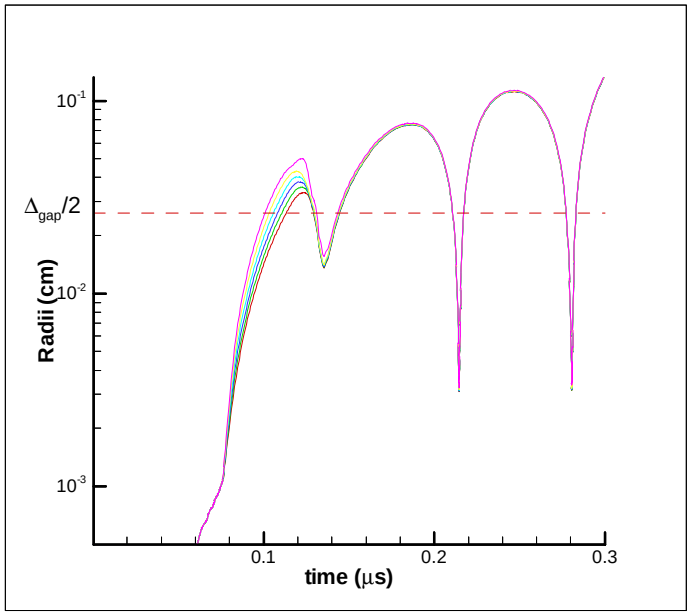

Figure 5-2: Outermost zone radii vs. time.

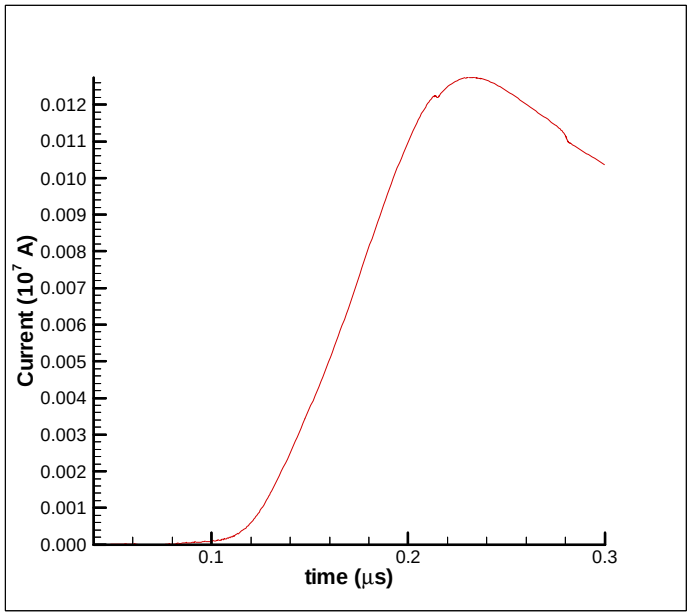

Figure 5-3: Current vs. time. Peak current occurs at approximately 0.2 μs.

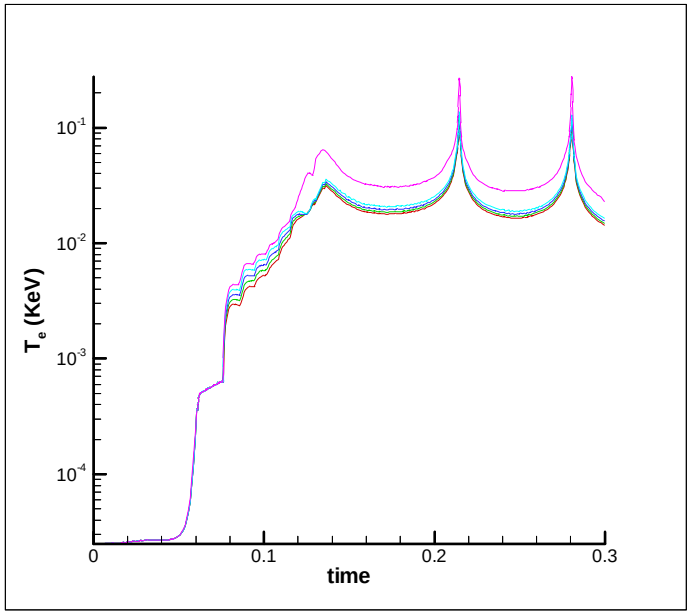

Figure 5-4: Electron temperature for outermost zones vs. time

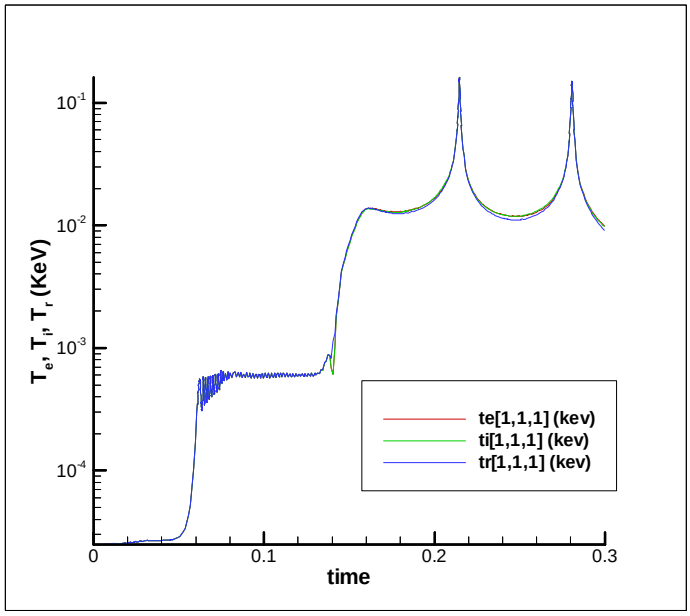

Figure 5-5: Innermost zone temperatures (T_e,T_i,T_r) vs. time.

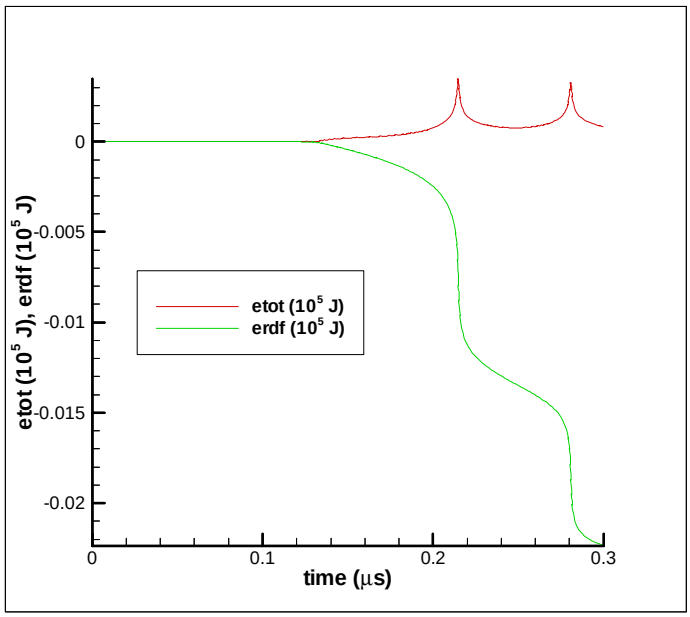

Figure 5-6: Plot of total energy radiated through boundary vs. time. Also shown is the total energy.

5.2.1 Contour Plots

We now look at several contours plots for the 1-D wire case discussed in the previous section. We will use a 3 times pre-expanded wire for this analysis since, for early times in the expansion phase, the bonding model produces an "accordion' like clumping of mass. The pre-expanded case is virtually indistinguishable from the "initiated from solid" case after the radiation wave has heated the inner zones of the wire. In either case, the radial expansion is the same as well as the bounce (repinch) times.

The density contours during the initial expansion of the wire are shown in figure 5-7. Contours at subsequent times are shown in figure 5-8. These show a repinching in the plasma in the low density corona at 140 and 150 ns. Shortly after this we see further expansion (170 ns). Figure 5-9 shows the radiation heating of the wire. Gradually, a radiation wave is sent through the core of the wire with the electron temperature lagging behind. This lag is shown in figure 5-10 where it is seen that radiation temperature is greater than the electron temperature in the wire core.

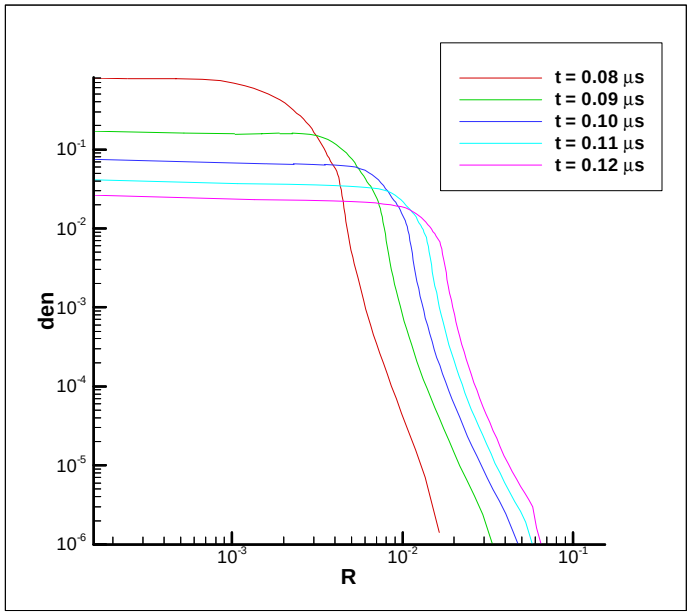

Figure 5-7: Density plots during expansion phase.

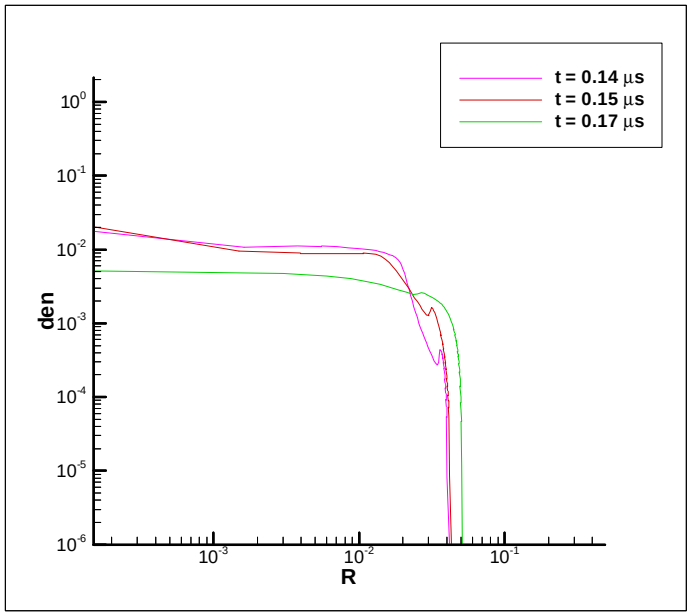

Figure 5-8: Density plots during and shortly after first repinch.

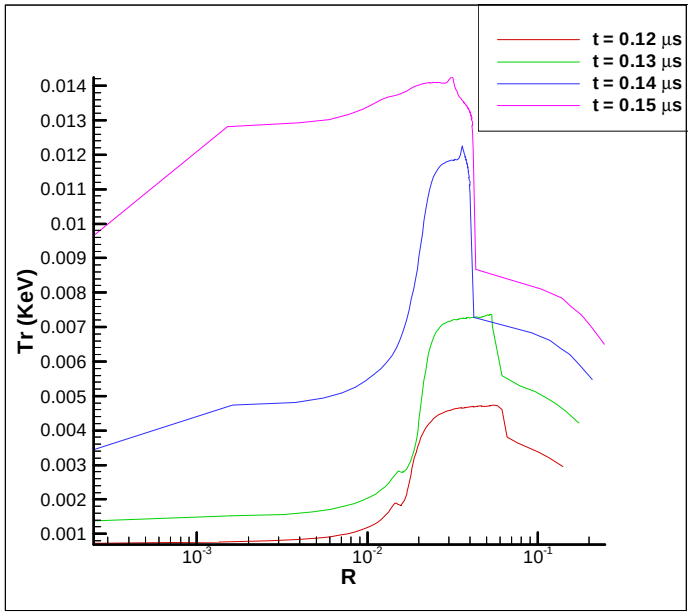

Figure 5-9: Radiation temperature plots.

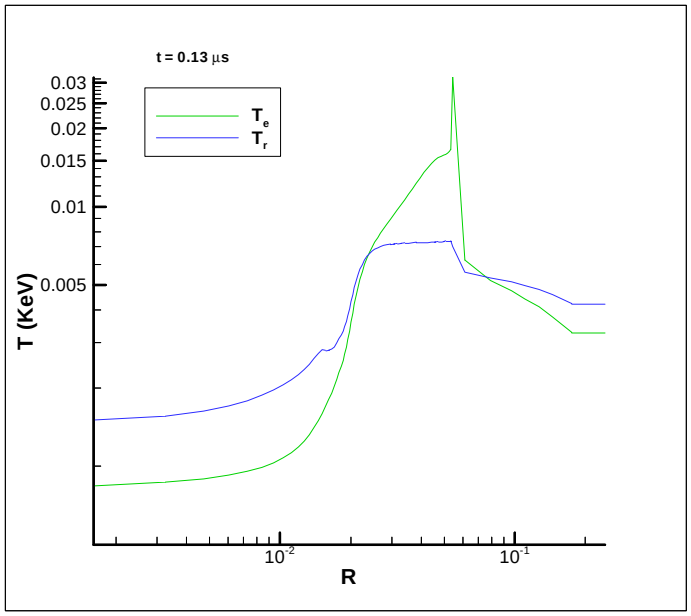

Figure 5-10: Radiation and Electron temperature at t = 0.13 μs

Chapter 6

RZ Plane Calculations

6.1 Motivation

Recent experiments have shown that the m=0 "sausage" instability is important in fiber Z-pinches. D. Kalantar showed that the plasma corona and inner core have different dynamics [20]. In his experiments with single aluminum wires he observed that only 1% of the wire mass formed a corona. The rest of the plasma was contained in a well-defined core. With X-pinch backlighting he showed that the instability growth of the corona, owing to its high Alfvén velocity, had a much more rapid growth rate than the inner core.

Because of the pronounced effect of the sausage instability on a single wire, we performed calculations on its effect on different wire diameters in a wire array. Specifically we performed a series of calculations for a 120 wire array at an initial radius of 2 cm on the PBFAZ machine. A plot of power output versus initial wire diameter (figure 6-1) shows a dramatic decrease in performance (measured in peak radiated power) - almost a factor of 3 - as wire diameter is increased [18]. As a first attempt to understand this curve we will study the sausage instability growth in individual wires of the array. The reasoning behind this is that growth of the sausage instability could seed the RT instability or otherwise degrade the performance of the Z-pinch.

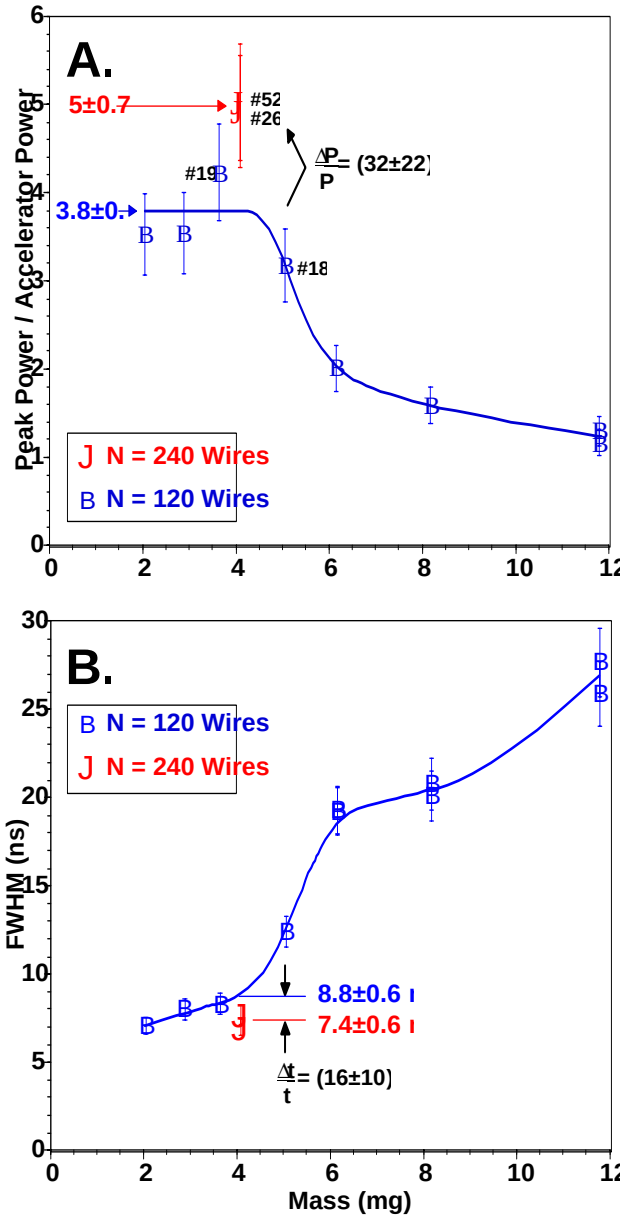

Figure 6-1: Ratio of peak total radiated power relative to peak electrical power measured at the insulator stack as a function of array mass, showing increase in radiated power near 4 mg when the number of wires is doubled, for the 20-mm radius array. Shot numbers are shown adjacent to the shots near array masses of 4 mg. (B) Radiation pulse width as a function of array mass, showing decrease in pulse width (FWHM) near 4 mg when the number of wires is doubled, for the 20-mm radius array.(Figure courtesy of Tom Sanford, SNL [18]).

6.2 Procedure

We considered four wire diameters: d=10, 11.8, 22, and 25.4 μm. As in the 1-D case, circuit parameters are appropriately scaled and the PBFAZ voltage waveform was used. The wire was initialized in 1-D until it expanded 10-20 times the original solid radius. This corresponded to a time of approximately 0.075 μs. Then the 1-D wire profile was mapped to a 2-D r-z plane mesh with an initial velocity perturbation.

The velocity perturbation was chosen to be a "sausage-type" mode periodic in the z-direction and satisfying incompressibility ($\nabla \cdot \overrightarrow{v_{pert}} = 0$):

$$\overrightarrow{v}_{pert} = (v_z, v_r) = \left[-\frac{2\varepsilon}{k} \sin(kz), \varepsilon r \cos(kz) \right] \tag{6.1}$$

where $k \equiv \frac{2\pi}{\lambda}$. This form is chosen because incompressibility is satisfied for ideal MHD modes near marginal stability.

We will model only a small segment of the wire (0.5 mm) and resolve only a half of a wavelength on it. This is chosen as a starting point since sausage modes of wavelength $\sim 1mm$ are seen in Kalantar's aluminum wire work.

To study the perturbation growth we must extract the growth rate, γ. Fourier transforming the velocity

$$v(k,t) = \sum \cos(kz)\, v(z)\, e^{i\omega t} dz \tag{6.2}$$

and the kinetic energy

$$\begin{aligned} KE(k,t) &= \frac{1}{2} \sum m v^2(k,t) = e^{2\omega_I t} \sum m \cos^2(kz)\, v^2(z)\, e^{i\omega t} dz \\ &= e^{2\gamma t} \sum m \cos^2(kz)\, v^2(z)\, e^{i\omega t} dz \end{aligned} \tag{6.3}$$

We see that the growth rate may be easily extracted from the Fourier transform of the kinetic energy:

$$\ln(KE(k,t)) = 2 \int \gamma dt + const. \tag{6.4}$$

Thus a plot of ln(KE) versus time will reveal the growth rate γ.

6.2.1 Test Case - Bennett Equilibrium

To illustrate this analysis we consider an ideal test with an analytic solution. We take a perfectly conducting Z-pinch in Bennett equilibrium with a small velocity perturbation. Bennett Equilibrium occurs when the magnetic pressure $B^2/8\pi$ is sufficient to balance the plasma pressure nK_BT. This leads to a condition on current. If we consider an ideally conducting cylindrical plasma the magnetic field at the surface is given by $B = 2I/r$. We may write the plasma pressure as

$$\begin{aligned} p &= p_e + p_i = n_e K_B T + n_i K_B T \\ &= (\overline{Z}+1) n K_B T = (\overline{Z}+1)\frac{N K_B T}{\pi r^2} \end{aligned}$$

where the electron temperature is assumed equal to the ion temperature ($T = T_e = T_i$) and N is the number of ions per unit length. Now, applying Ampere's law and pressure balance we obtain

$$\frac{B^2}{8\pi} = (Z+1)\frac{N K_B T}{\pi r^2}$$

$$\frac{1}{8\pi}\left(\frac{2I}{r}\right)^2 = (Z+1)\frac{N K_B T}{\pi r^2}$$

$$I^2 = 2(Z+1) N K_B T \tag{6.5}$$

This is the Bennett pinch condition. In Chapter 9 we will present another type of equilibrium condition for Z-pinches.

Unlike the velocity perturbation presented earlier, only the outer zones (in the r-direction) will be perturbed:

$$\overrightarrow{v}_{pert} = (v_z, v_r) = [0, v_o \cos(kz)] \tag{6.6}$$

The analytic solution to the growth rate for this problem is given by [1][2]:

$$\gamma^2 = -\omega^2 = \frac{B_\phi^2}{4\pi\rho_o r^2} Kr \frac{I_o'(Kr)}{I_o(Kr)} \tag{6.7}$$

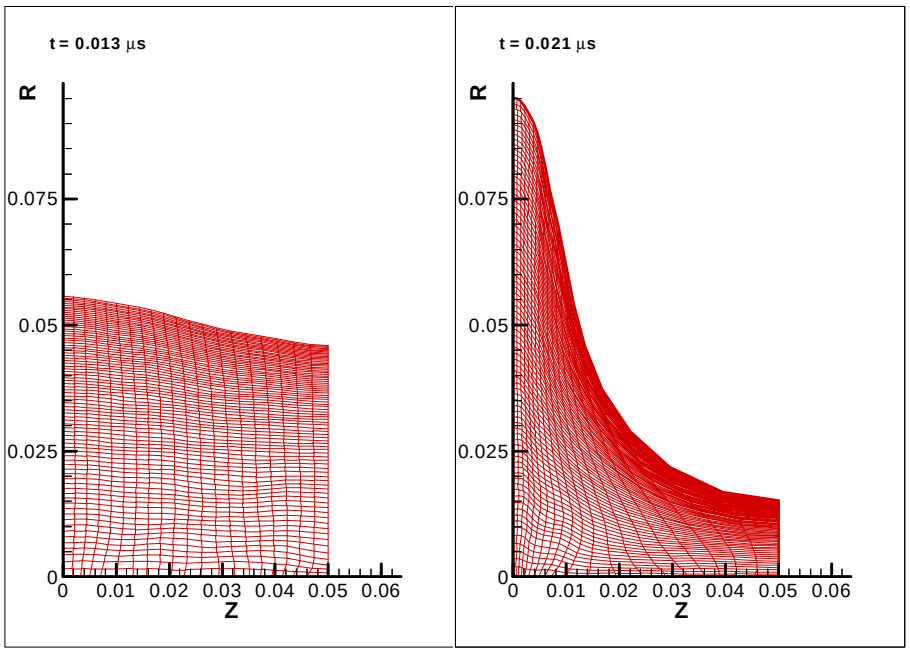

Figure 6-2: Mesh plots showing growth of sausage mode perturbation. Half a wavelength is resolved on the mesh.

where, writing the sound speed as $(\gamma P_o/\rho_o)^{1/2} = c_s^2$,

$$K^2 = k^2 \left[1 - \frac{(\omega/k)^2}{c_s^2} \right] \tag{6.8}$$

For our test example we take $r_o = .05\ cm$, $\rho = 1.93 \times 10^{-3}\ g/cc$, $T_e = T_i = 100\ eV$. We use the ideal gas EOS, which is assumed in the Bennett model, with $\overline{Z} = 74$, $\overline{A} = 183.85$ (fully ionized tungsten). To maintain Bennett equilibrium we apply a current of 0.344 MA ($B_\phi = 1.38\ MG$) to the wire. 0ur velocity perturbation is $v_o = 0.05\ cm/\mu s$ with a wavelength of $\lambda = 1\ mm$. From a linear fit of the plot of ln(KE) vs. time we find a growth rate of $\gamma \approx 250\ 1/\mu s$. The analytic solution (solved with Mathematica) gives $\gamma = 258\ 1/\mu s$. Several meshes of increasingly finer resolution were used until the growth rate, which scales as N_{zones}^{-2}, converged. We see that Trac-II agrees fairly well with the analytic value. Some discrepancy is probably due to an artificial pressure that is introduced to prevent mesh distortions.

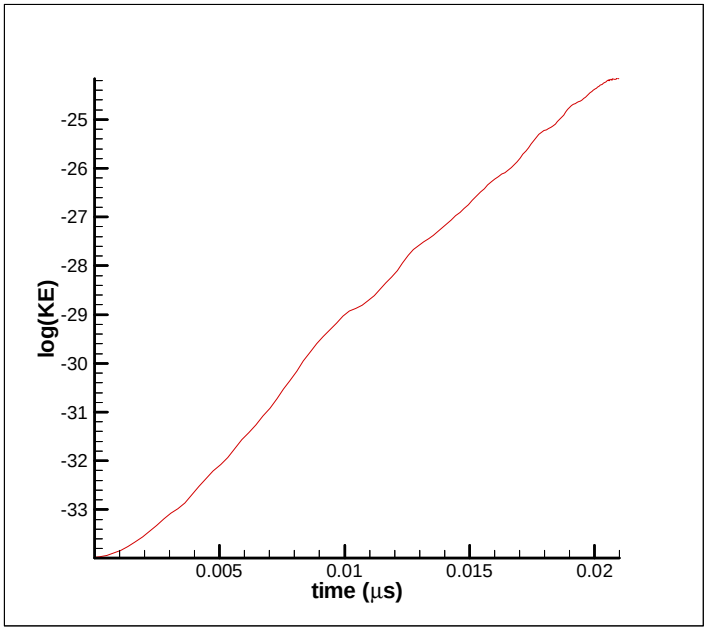

Figure 6-3: Plot of $\ln[KE(k,t)]$ vs. time. The wire undergoes approximately 5 e-foldings.

6.3 Tungsten Wire Runs

6.3.1 Short Wavelength Results

As mentioned before, we consider Tungsten wires of initial diameters d=10, 11.8, 22, and 25.4 μm. The 2-D run is initiated (from its 1-D counterpart) at $t_o = 0.075\ \mu s$. The perturbation velocity $v_o = \varepsilon r$ is chosen to be 1% of the maximum expansion velocity ($v_o = 0.03\ cm/\mu s$). The perturbation wavelength is taken to be $\lambda = 1\ mm$ on a mesh of length $0.5\ mm$ in the z-direction. The code is run in pure Lagrangian mode and the mesh tangles or "bowties" at about $t \approx 0.15\ \mu s$ for each wire case. At that point the run is terminated.

Unfortunately, an infinitesimally small (i.e. $1 \times 10^{-8}\ cm/\mu s$) perturbation could not be chosen since the thermal and toroidal magnetic field diffusion routines use the "operator splitting" or ADI method [9]. This method, which involves dividing the timestep into two steps of size $\Delta t/2$ and solving each direction implicitly with a trivial tridiagonal matrix inversion, introduces noise into the calculation. In the future, these routines will be converted

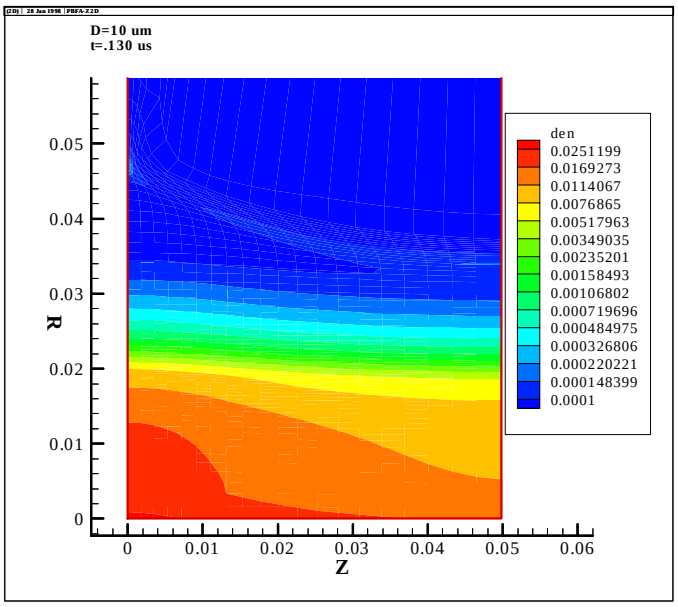

Figure 6-4: Contour plot of density for 10 μm wire.

to a fully implicit solution with ICCG (as done for the radiation and poloidal magnetic field diffusion).

Contour plots of density taken late into the calculation are shown in figures 6-4 and 6-5. Also shown (figures 6-6 and 6-7) are contour plots of magnetic field B_ϕ as well as electron temperature.

6.3.2 Analysis

Next we examine the sausage mode perturbation growth for the Tungsten wires. During the first 40 ns each wire freely expands due to ohmic heating and there is little perturbation growth. In the subsequent $40 - 60$ ns the wire undergoes its first pinch and the growth is rapid - approximately $200 - 250$ $1/\mu s$ for each wire. This is due to the fact that magnetic pressure increases and radiative losses reduce the electron pressure of the wire. In each wire there are about 4-5 e-foldings before mesh distortions force the run the stop. Comparing growth rates between wires we see that there is not an appreciable difference between large

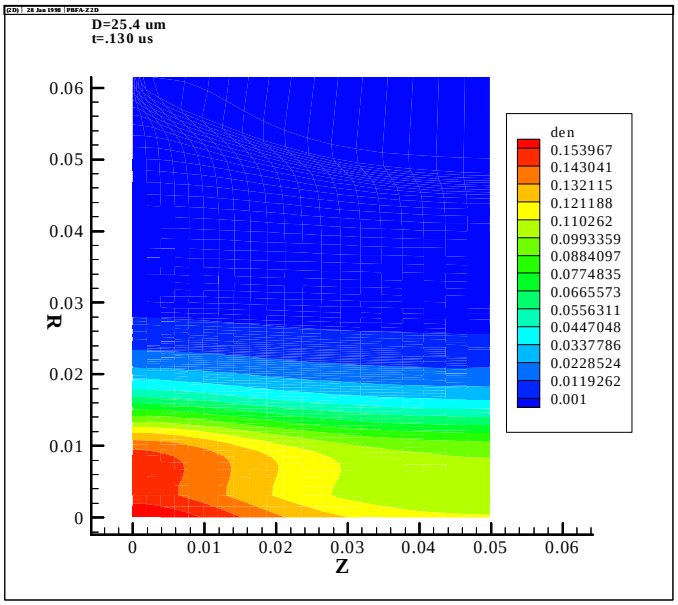

Figure 6-5: Contour plot of density for 25.4 μm wire.

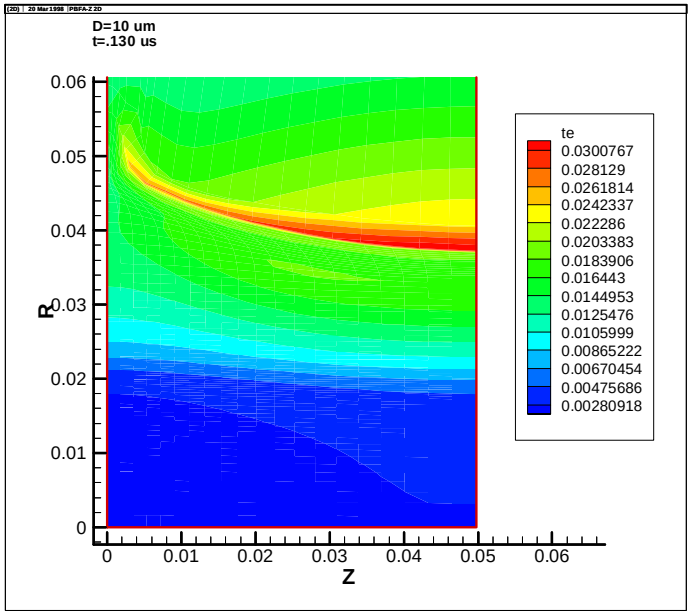

Figure 6-6: Contour plot of T_e (KeV) for a 10 μm wire.

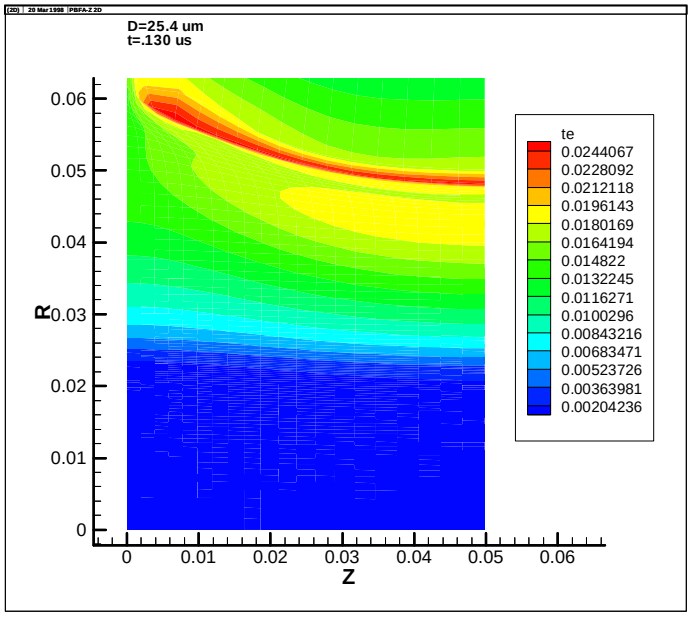

Figure 6-7: Contour plot of T_e (KeV) for a 25.4 μm wire.

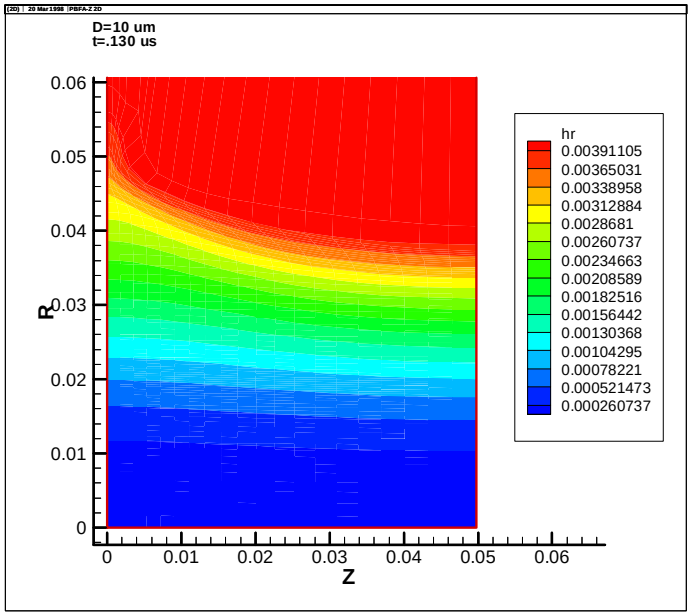

Figure 6-8: Contour plot of rB_ϕ $(MG \cdot cm)$ for a 10 μm wire.

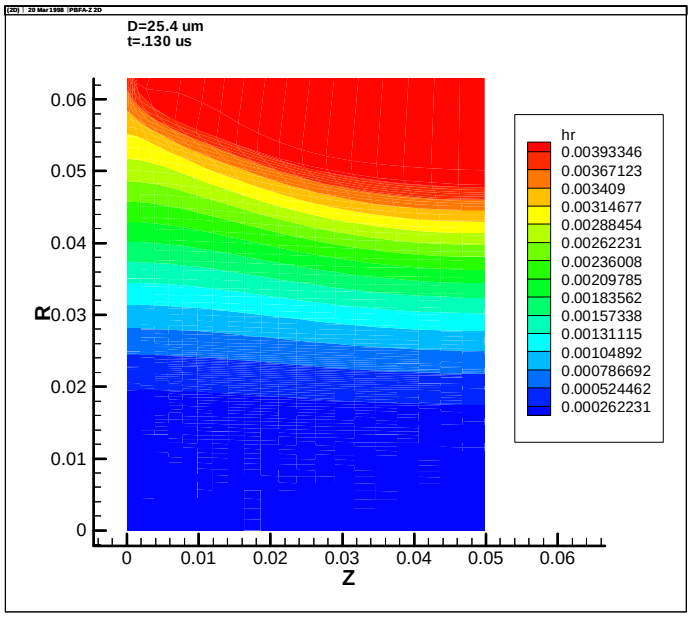

Figure 6-9: Contour plot of rB_ϕ $(MG \cdot cm)$ for a 25.4 μm wire.

and small wires. Figure 6-10 indicates that slopes the ln(KE) vs. time curves, which are equal to 2γ, are approximately the same. Thus it does not appear that sausage mode growth is responsible for the dramatic bend in the power curve.

Some further insight in to this result can be provided by looking at the "half-current radius" for these four wires in 1-D. This is defined as the radius which encloses half the total current of the wire. Figure 6-11 shows that the time histories for the various initial wire radii are nearly the same. This shows that the 1-D dynamics of the outer plasma of the wire does not seem to vary significantly with wire radius. Since to first order Alfvén and sound speed determine growth rate, this is consistent with our 2-D calculations. Furthermore, we see that the radius of the expanding plasma does not quite exceed half the gap distance $(\Delta_{gap}/2)$. This suggests that wires in the 120 wire array are able to repinch and develop a sausage mode.

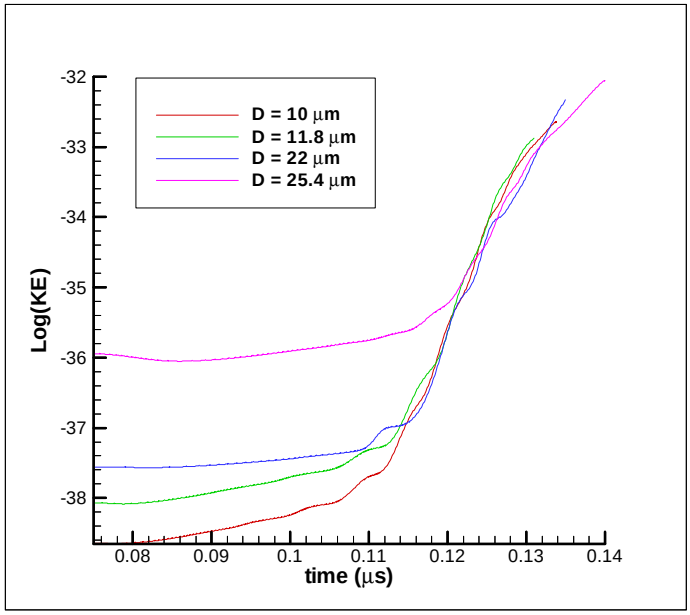

Figure 6-10: Plot of ln(KE) vs. time for various wire radii.

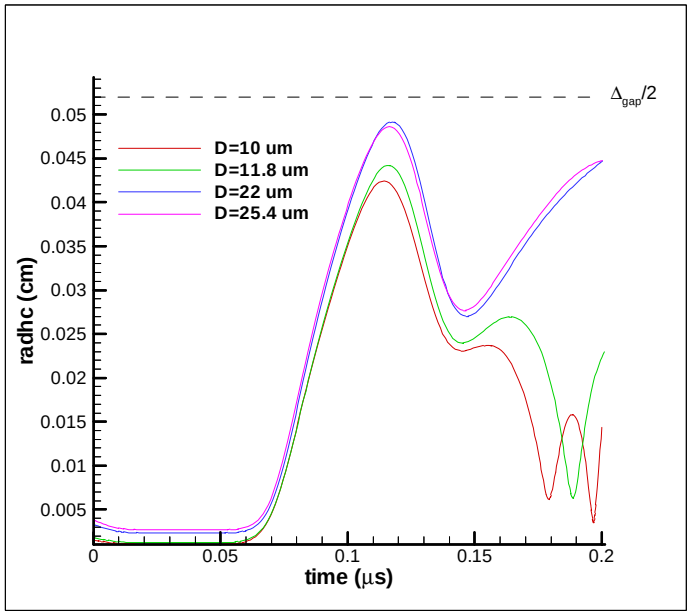

Figure 6-11: "Half Current" vs time for various wire radii.

6.3.3 Long Wavelength Results

Lastly we consider long wavelength ($\lambda = 4\ mm$) perturbations in both large and small diameter wires. In these runs we shall use a floor density of $\rho_{\min} = 2 \times 10^{-6}\ g/cc$ in a slightly different way than before. Instead of defaulting $\eta = \infty$ when $\rho < \rho_{\min}$, we shall add mass to the zone so it does not fall beneath the floor value. The velocity perturbation takes the same form as in the previous section but is larger (10% of maximum velocity or $v_o = 0.3\ cm/\mu s$). The runs are initiated at $t_o = 0.1\ \mu s$.

Density contours are shown in figures 6-11 and 6-12 for a 10 and 18 μm wire at approximately the same time in the current pulse. These are taken during the first recompression. In these runs we find that the calculation can proceed even after the first repinch. The plots of Log(KE) for both wires (figure 6-14) show that they have roughly the same growth rate during the first repinch ($\gamma \approx 80\ 1/\mu s$). The smaller wire experiences a second and more rapid repinch before the larger wire and this is reflected in the differences in the growth rate after 0.14 μs.

Unlike the shorter wavelength ($\lambda = 1\ mm$) case, the wires only undergo about one e-folding by the time of the first repinch (0.14 μs). We conclude that longer wavelengths become less important in terms of sausage instability growth. Using the analytic growth rate formula (equation 6.7) as an estimate, we see that for long wavelength (or small kr) the growth rate scales inversely with wavelength ($\gamma \sim 1/\lambda$). The scaling is not quite as strong in the cases shown here but it should be noted that equation 6.7 is derived with the assumption of an ideally conducting plasma initially in equilibrium and neglecting diffusion effects.

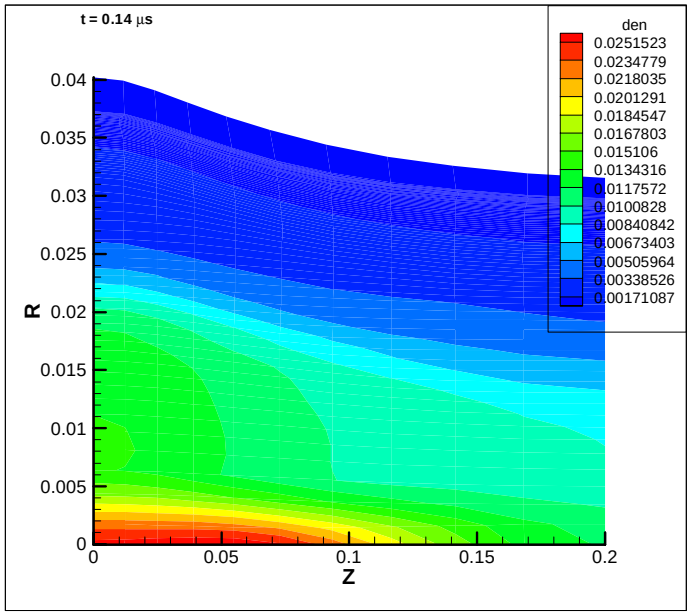

Figure 6-12: Density contour plot for 18 μm wire in a 120 wire array.

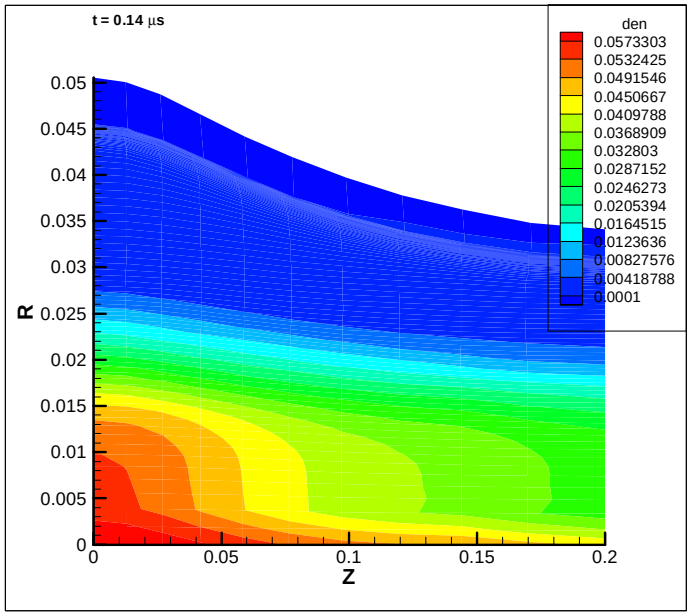

Figure 6-13: Density contour plot for 10 μm wire in a 120 wire array.

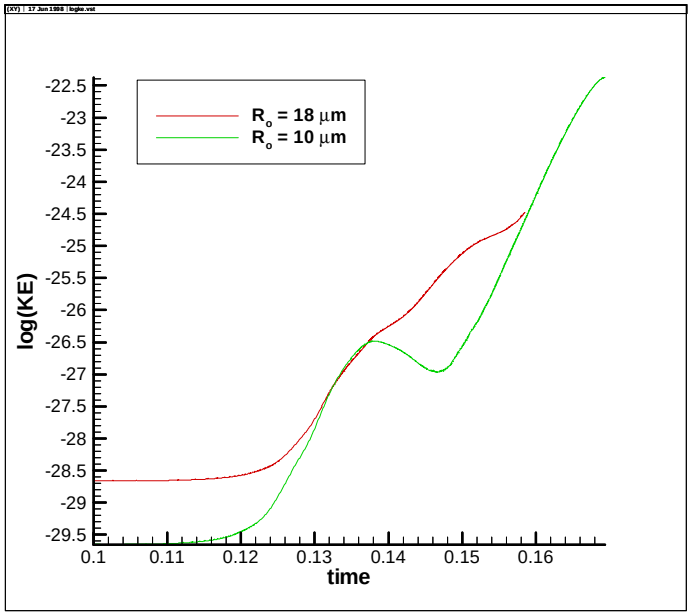

Figure 6-14: Plot of ln(KE) vs. time for long wavelength ($\lambda = 4\ mm$) perturbations.

Chapter 7

Poloidal Magnetic Field Diffusion

7.1 Introduction

Trac-II solves all three components of the magnetic field (B_z, B_r, B_ϕ). However, until recently the diffusion of the poloidal part of the magnetic field $(\overrightarrow{B_p} = (B_z, B_r))$ was solved explicitly. Therefore, the timestep was limited by the Courant condition for magnetic field diffusion:

$$\triangle t \leq \frac{4\pi}{\eta} \triangle x^2 \tag{7.1}$$

In the $r - \vartheta$ plane wire array problem it is necessary to introduce vacuum regions around the wire. Usually these regions are filled with low density, high resistivity material. The magnetic field will pass through this low density material and establish itself around the wire. To do this most effectively an implicit diffusion scheme, stable for any timestep, must be used. Then the resistivity in the vacuum may be set to infinity and the magnetic field will establish itself instantaneously around the wire. In contrast, an explicit scheme would require that the magnetic field be passed artificially slowly through the vacuum. This generally results in spurious heating and large magnetic pressure gradients in the vacuum region.

Thus it was necessary to derive and implement an implicit diffusion scheme for the poloidal magnetic field. This was done to be consistent with the definitions of magnetic field and current already in Trac-II. Furthermore, the scheme is general to a non-orthogonal

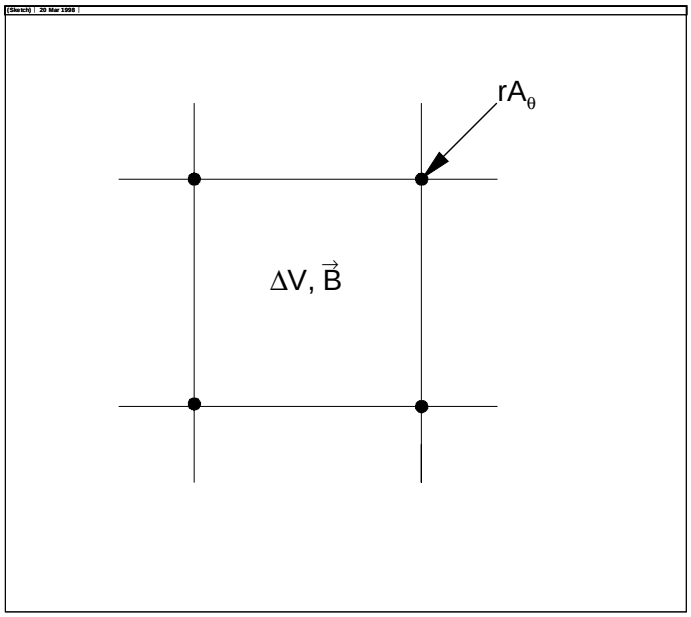

Figure 7-1: Single zone. Note that $\overrightarrow{B}$ is "zone centered" whereas rA_θ is "node centered".

moving mesh.

7.2 Magnetic Field and Current

We must first describe how poloidal magnetic field and the associated azimuthal current are defined in Trac-II. Consider a single zone in a mesh (figure 7-1).

Magnetic field may be derived from the vector potential:

$$\overrightarrow{B} = \nabla \times \overrightarrow{A} \tag{7.2}$$

In our single zone we may find $\overrightarrow{B}$ through Stokes Law for an incremental volume $\triangle V$

$$\begin{aligned} \overrightarrow{B}_p \Delta V &= \int \nabla \times \overrightarrow{A}\, dV \\ &= \oint \overrightarrow{dS} \times \overrightarrow{A} = \oint \left(-\widehat{\theta} \times r\overrightarrow{dl} \right) \times \overrightarrow{A} \\ &= -\oint (rA_\theta)\, \overrightarrow{dl} \end{aligned} \tag{7.3}$$

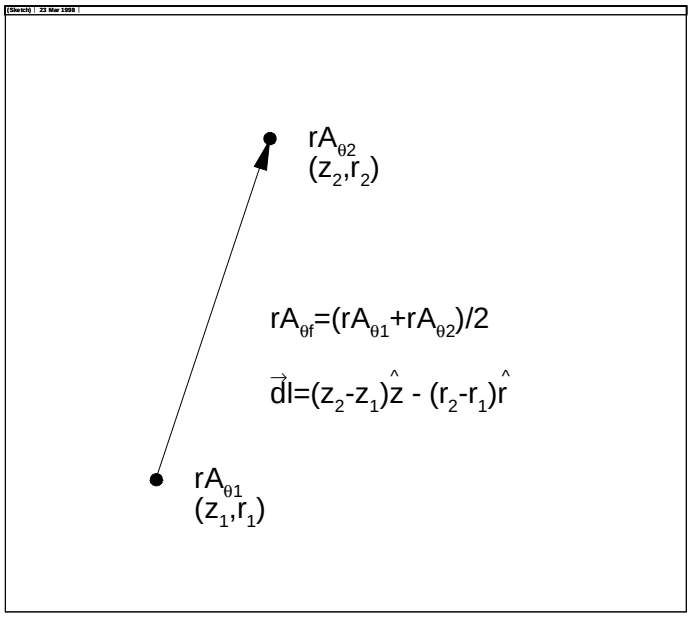

Figure 7-2: Definition of rA_θ on faces used to calculate $\overrightarrow{B}$.

rA_θ will be our fundamental variable defined on the nodes of our mesh. $\overrightarrow{B}$ will be calculated using the value of rA_θ on the zone faces (taken as the average of rA_θ along the adjoining nodes) along with the length vector $\overrightarrow{dl}$ which connects the two nodes on each face. This is shown in figure 7-2.

Thus we may write

$$\overrightarrow{B}_p = -\frac{1}{\Delta V} \sum \left(rA_\theta\right)_f \overrightarrow{dl}_f \tag{7.4}$$

Note that magnetic field is a zonal quantity. Current density $J_{\theta,n}$ is defined as a nodal quantity. It is found by using Ampere's law at each face to find the current I_f (figure 7-3) and then apportioning the current to each node according to

$$J_{\theta,n} = \frac{1}{2A_n} \sum I_f \tag{7.5}$$

A_n is simply the "nodal" area - the average of the areas of the four zones surrounding node n.

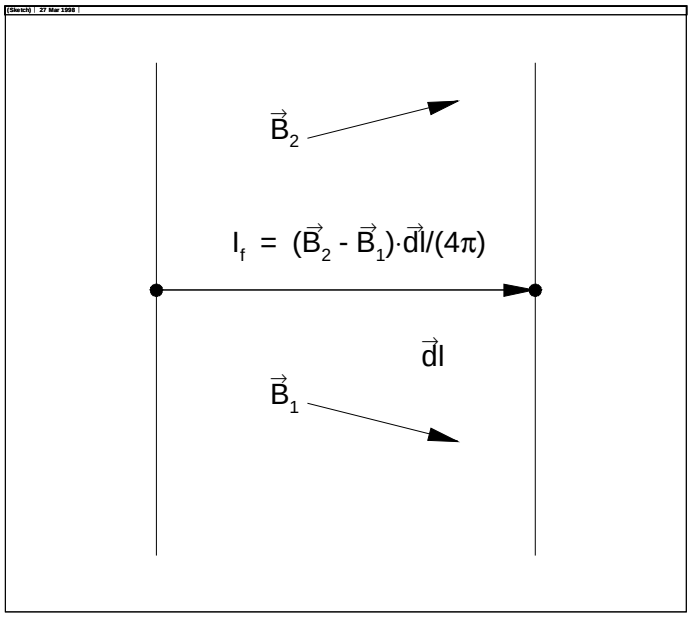

Figure 7-3: Definition of face current I_f

7.3 Magnetic Diffusion

Using Faraday's law:

$$\frac{\partial \overrightarrow{B}}{\partial t} = -\nabla \times \overrightarrow{E} \tag{7.6}$$

and integrating around an area $\overrightarrow{da}$ we obtain

$$\int \frac{\partial \overrightarrow{B}}{\partial t} \cdot \overrightarrow{da} = \frac{\partial}{\partial t}\Phi = -\int \nabla \times \overrightarrow{E} \cdot \overrightarrow{da} = -\oint \overrightarrow{E} \cdot \overrightarrow{dl} \tag{7.7}$$

Using Ohm's Law

$$\overrightarrow{E} = \eta \overrightarrow{J} \tag{7.8}$$

we obtain

$$\begin{aligned} \frac{\partial}{\partial t}\Phi &= -\oint \eta \overrightarrow{J} \cdot \overrightarrow{dl} \\ &= -\langle \eta \rangle \oint \overrightarrow{J} \cdot \overrightarrow{dl} \end{aligned} \tag{7.9}$$

where $\langle\eta\rangle$ is an appropriately averaged quantity that we will define later.

Now we use the fact that our magnetic fields are poloidal ($\overrightarrow{B_p} = (B_z, B_r)$) and thus our current density lies only in the $\widehat{\theta}$ direction ($\overrightarrow{J} = J_\theta\ \widehat{\theta}$). We may do the integration over $\overrightarrow{dl}$ easily due to axisymmetry

$$\frac{\partial}{\partial t}\Phi = 2\pi r \langle\eta\rangle J_\theta \tag{7.10}$$

Flux is simply related to vector potential in cylindrical coordinates

$$\begin{aligned} \Phi &= \int \overrightarrow{B_p}\cdot\overrightarrow{da} = \int \nabla\times\overrightarrow{A}\cdot\overrightarrow{da} = \int \frac{1}{r}\frac{\partial}{\partial r}(rA_\theta)\, r dr d\theta \\ &= 2\pi r A_\theta \end{aligned} \tag{7.11}$$

Finally we may write our diffusion equation

$$\frac{\partial}{\partial t}(rA_\theta) = -r\langle\eta\rangle J_\theta \tag{7.12}$$

7.4 Implicit Diffusion

Now we will derive an implicit solution to our diffusion equation. Writing equation 7.12 in implicit form we obtain

$$(rA_\theta)^{n+1}_{i,j} - (rA_\theta)^n_{i,j} = -\triangle t r_{i,j}\langle\eta\rangle J^{n+1}_{\theta i,j} \tag{7.13}$$

Next we find the current at each node $J^{n+1}_{\theta i,j}$. Our face length vectors are illustrated in figure 7-4 and with the definition of current density given in equation 7.5 we have

$$\begin{aligned} J^{n+1}_{\theta i,j} &= \frac{1}{8\pi A_{i,j}}\{\left(\overrightarrow{B}_{i,j-1} - \overrightarrow{B}_{i,j}\right)\cdot\overrightarrow{dh}_{i,j} - \left(\overrightarrow{B}_{i,j} - \overrightarrow{B}_{i-1,j}\right)\cdot\overrightarrow{dv}_{i,j} - \\ &\quad \left(\overrightarrow{B}_{i-1,j-1} - \overrightarrow{B}_{i-1,j}\right)\cdot\overrightarrow{dh}_{i-1,j} - \left(\overrightarrow{B}_{i,j-1} - \overrightarrow{B}_{i-1,j-1}\right)\cdot\overrightarrow{dv}_{i,j-1}\} \end{aligned} \tag{7.14}$$

We may also write all the $\overrightarrow{B}$ in terms of the vector potentials ($b_{i,j} \equiv (rA_\theta)_{i,j}$) at each of the 9 nodes in the mesh shown in figure 7-4.

$$\overrightarrow{B}_{i,j} = \frac{1}{2\Delta V_{i,j}}\{-(b_{i,j} + b_{i+1,j})\cdot\overrightarrow{dh}_{ij} - (b_{i+1,j} + b_{i+1,j+1})\cdot\overrightarrow{dv}_{i+1,j}$$

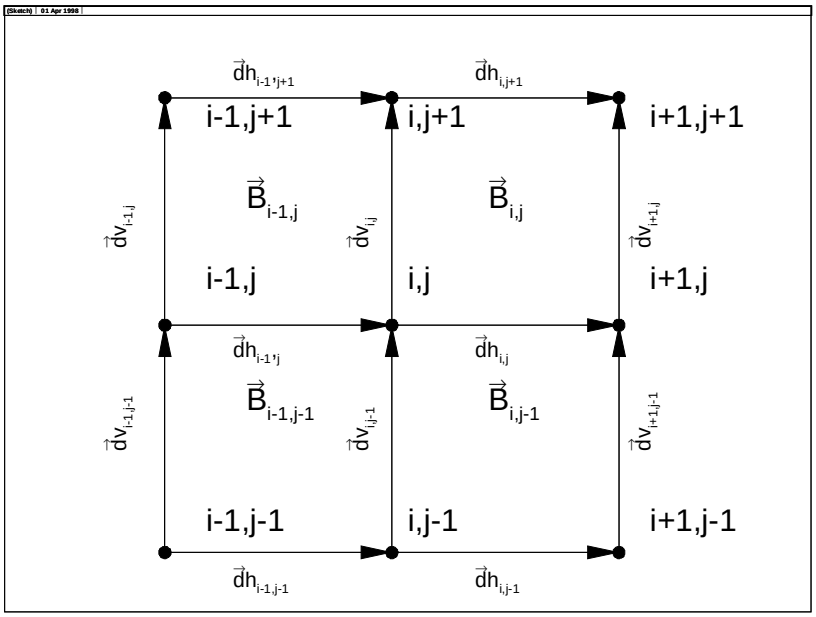

Figure 7-4: Computational grid for deriving difference scheme.

$$
\begin{aligned}
& + (b_{i,j+1} + b_{i,j+1}) \cdot \overrightarrow{dh}_{i,j+1} + (b_{i,j+1} + b_{i,j}) \cdot \overrightarrow{dv}_{i,j} \} \\
\overrightarrow{B}_{i-1,j} &= \frac{1}{2\Delta V_{i-1,j}} \{ - (b_{i-1,j} + b_{i,j}) \cdot \overrightarrow{dh}_{i-1,j} - (b_{i,j} + b_{i,j+1}) \cdot \overrightarrow{dv}_{i,j} \\
& + (b_{i,j} + b_{i-1,j+1}) \cdot \overrightarrow{dh}_{i-1,j+1} + (b_{i-1,j+1} + b_{i-1,j}) \cdot \overrightarrow{dv}_{i-1,j} \} \\
\overrightarrow{B}_{i,j} &= \frac{1}{2\Delta V_{i-1,j-1}} \{ - (b_{i-1,j-1} + b_{i,j-1}) \cdot \overrightarrow{dh}_{i-1,j-1} - (b_{i,j-1} + b_{i,j}) \cdot \overrightarrow{dv}_{i,j-1} \\
& + (b_{i,j} + b_{i-1,j}) \cdot \overrightarrow{dh}_{i-1,j} + (b_{i-1,j} + b_{i-1,j-1}) \cdot \overrightarrow{dv}_{i-1,j-1} \} \\
\overrightarrow{B}_{i,j-1} &= \frac{1}{2\Delta V_{i,j-1}} \{ - (b_{i,j-1} + b_{i+1,j-1}) \cdot \overrightarrow{dh}_{i,j-1} - (b_{i+1,j-1} + b_{i+1,j}) \cdot \overrightarrow{dv}_{i+1,j-1} \\
& + (b_{i+1,j} + b_{i,j}) \cdot \overrightarrow{dh}_{i,j} + (b_{i,j} + b_{i,j-1}) \cdot \overrightarrow{dv}_{i,j-1} \} \qquad (7.15)
\end{aligned}
$$

We may combine equation 7.14 and 7.15 to obtain a 9-point difference scheme in the form

$$
\begin{aligned}
b_{i,j}^{n+1} - b_{i,j}^{n} &= c_{i-1,j-1} b_{i-1,j-1} + c_{i,j-1} b_{i,,j-1} + c_{i+1,j-1} b_{i+1,j-1} \\
& c_{i-1,j} b_{i-1,j} + c_{i,j} b_{i,j} + c_{i+1,j} b_{i+1,j} \\
& c_{i-1,j+1} b_{i-1,j+1} + c_{i,j+1} b_{i,j+1} + c_{i+1,j+1} b_{i+1,j+1} \qquad (7.16)
\end{aligned}
$$

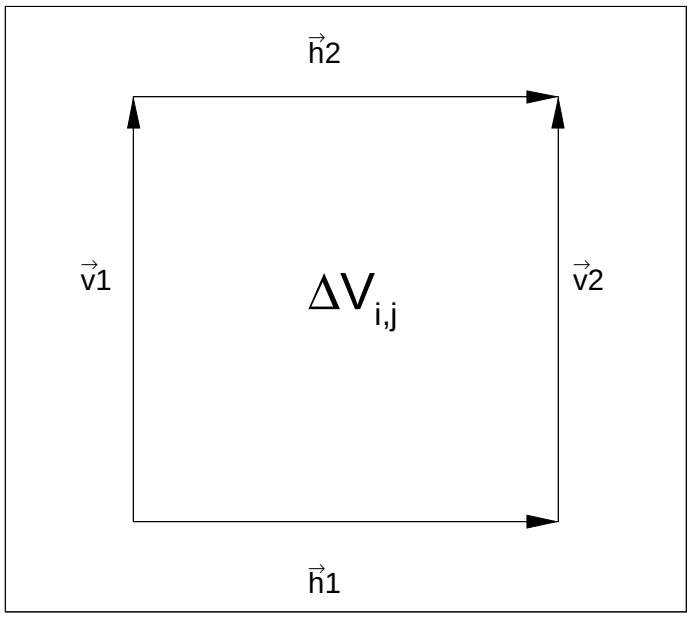

Figure 7-5: Shorthand for "face vectors".

Next we define a shorthand for the "face vectors" in each zone as shown in figure 7-5. The coefficients are given by:

$$
\begin{aligned}
c_{i-1,j-1} &= \left[\frac{\alpha}{2V}\left(-h1h2 + h2v1 + h1v2 - v1v2\right)\right]_{i-1,j-1} \\
c_{i,j-1} &= \left[\frac{\alpha}{2V}\left(-h1h2 - v2h2 + h1v2 + v2v2\right)\right]_{i-1,j-1} \\
&\quad + \left[\frac{\alpha}{2V}\left(-h1h2 + h2v1 - v1h1 + v1v1\right)\right]_{i,j-1} \\
c_{i+1,j-1} &= \left[\frac{\alpha}{2V}\left(-h1h2 - v2h2 - v1h1 - v1v2\right)\right]_{i+1,j-1} \\
c_{i-1,j} &= \left[\frac{\alpha}{2V}\left(h1v2 - v1v2 - h1h1 - v1h1\right)\right]_{i-1,j} \\
&\quad + \left[\frac{\alpha}{2V}\left(h2h2 + h2v1 - v2h2 - v1v2\right)\right]_{i-1,j-1} \\
c_{i,j} &= \left[\frac{\alpha}{2V}(h2h2 + 2h2v1 + v1v1)\right]_{i,j-1} \\
&\quad + \left[\frac{\alpha}{2V}\left(h1h1 - 2v1h1 + v1v1\right)\right]_{i,j} \\
&\quad + \left[\frac{\alpha}{2V}\left(h1h1 + 2h1v2 + v2v2\right)\right]_{i-1,j} \\
&\quad + \left[\frac{\alpha}{2V}\left(h2h2 - 2v2h2 + v2v2\right)\right]_{i-1,j-1}
\end{aligned}
$$

$$
\begin{aligned}
c_{i+1,j} &= \left[\frac{\alpha}{2V}\left(-v2h2 + h2h2 - v1v2 - h2v1\right)\right]_{i,j-1} \\
&\quad + \left[\frac{\alpha}{2V}\left(h1h1 + h1v2 - v1h1 - v1v2\right)\right]_{i,j} \\
c_{i-1,j+1} &= \left[\frac{\alpha}{2V}(-v2h2 - v1v2 - h1h2 - v1h1\right]_{i-1,j} \\
c_{i,j+1} &= \left[\frac{\alpha}{2V}\left(-h1h2 - v1h1 + h2v1 + v1v1\right)\right]_{i,j} \\
&\quad + \left[\frac{\alpha}{2V}\left(v2v2 - v2h2 + h1v2 - h1h2\right)\right]_{i-1,j} \\
c_{i+1,j+1} &= \left[\frac{\alpha}{2V}\left(h1v2 - h1h2 - v1v2 + h2v1\right)\right]_{i,j}
\end{aligned} \tag{7.17}
$$

where

$$
\alpha \equiv \alpha_{i,j} = \frac{r_{i,j}\left\langle \eta \right\rangle_{i,j}}{8\pi A_{i,j}} \tag{7.18}
$$

7.5 Ohmic Heating

To derive the ohmic heating formula we look at the energy change of the magnetic field at each node:

$$
\begin{aligned}
\delta U_{B,n} &= \frac{1}{4\pi}\sum \overrightarrow{B}_p \cdot \delta\left(B_p \Delta V\right) \\
&= -\frac{1}{4\pi}\sum \overrightarrow{B}_p \cdot \oint \delta b_n \overrightarrow{dl} \\
&= -\frac{1}{4\pi}\delta b_n \sum \overrightarrow{B}_p \cdot \overrightarrow{dl} \\
&= -\delta b_n J_{\theta,n} A_n
\end{aligned} \tag{7.19}
$$

Next we distribute the ohmic heating to the nodes according to our area-weighted conductivity

$$
\delta U_{B,v} = \sum \frac{\sigma_v A_v}{4\sigma_n A_n}\delta U_{B,n} = -\delta U_{ee,n} \tag{7.20}
$$

Chapter 8

The Wire Array Z-pinch

8.1 Background

We now turn our attention to the $r-\vartheta$ plane of the wire array. We will attempt to study the merging of neighboring wires. An initially uniform shell is assumed in many $r-z$ plane Rayleigh-Taylor instability calculations. An $r-\vartheta$ calculation could be used to determine when this shell is formed (and if it is formed) along with its density and temperature profile. Thus a calculation of this type would more accurately determine the initial conditions for the RT calculations. Furthermore, the characteristics of merging for arrays of different wire number or wire diameter might elucidate the dramatic knees seen in the power curves.

In this chapter we present our method for modeling the $r-\vartheta$ plane of the wire array. We discuss several calculations that illustrate the behavior of the merging wires. Finally, we reconsider the 120 wire array shots studied in the previous section to determine if the bend in the power curve can be attributed to merging characteristics in the $r-\vartheta$ plane,

8.2 Computational Setup

The $r-\vartheta$ calculation is accomplished by translating the $r-z$ mesh to large radius so that essentially planar coordinates are obtained. A cross section of the wire (figure 8-1) is a large "bicycle tire" wrapped around the z-axis. Since we are concerned with the merging of neighboring wires, we shall only consider a single wire with mirror boundary conditions.

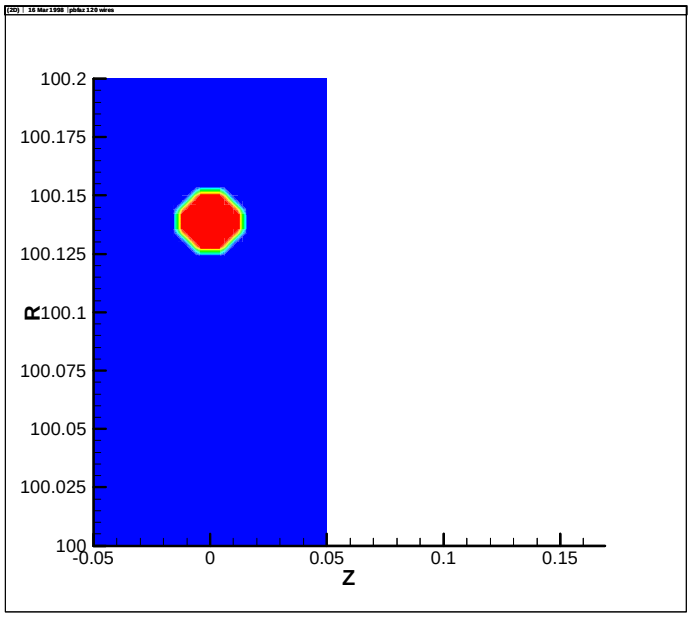

Figure 8-1: Single wire in "$r-\theta$" plane.

This can be represented by half of a wire at one boundary with a mesh width equal to half the gap distance (figure 8-2).

Because we are interested in small displacements of the wire towards the wire array axis, we first consider a "planar" array of wires. This approximates the circular array while $\triangle_{gap}/R_{array} \ll 1$ fairly well. Later we bend the boundaries in slightly, producing the appropriate "wedge" geometry. Essentially we will be studying a segment of the wire array in xy coordinates since we are not presently interested in following the wires down to convergence on the axis.

The system is driven by a load voltage determined by a 1-D array run from LASNEX. This voltage drives the flux at the upper boundary, rA_θ, according to Faraday's Law:

$$\frac{\partial}{\partial t} rA_\theta = -\frac{1}{2\pi} V_{load}\left(t\right) \tag{8.1}$$

Since large distortions of the mesh would occur during expansion, we run the problem in pure Eulerian mode.

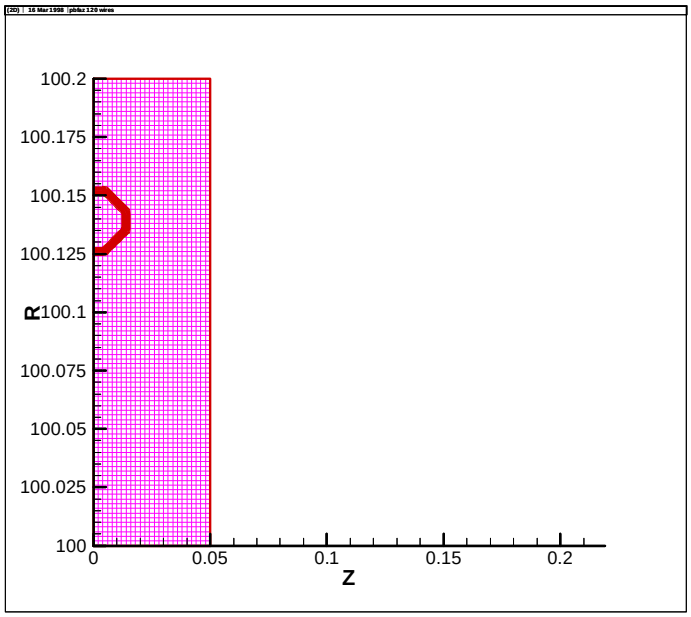

Figure 8-2: Computational mesh

8.3 Initial Examples of R-θ Calculations

As an initial test case we consider a 20 times pre-expanded 10 μm Tungsten wire from a 180 wire array. We set the conductivity to be an artificially high value (ideal MHD) and turn off radiation. Density, current density, and magnetic flux contour plots are shown in figures 8-3 to 8-6. These plots are taken at about 0.047 μs into the calculation which was initiated at 0.1 μs. During this time the wire has moved approximately 1 mm towards the axis. This is small compared to the initial radius of the wire array (20 mm).

As figure 8-3 indicates, the dynamics of the wire in the array is quite different than that of a single wire Z-pinch. Because of magnetic pressure, low density material in the wire gap is propelled towards the axis. The resulting wire takes on a teardrop shape. Clearly a single wire in an array does not remain radially symmetric

Next we consider a more realistic example. We consider a single 10 μm wire in an 180 wire array. The wire is pre-expanded 20 times in radius and, as before, the PBFA-Z load voltage is applied to the upper boundary. The problem is initiated at $t_o = 0.1$ μs. In this case both radiation diffusion and resistivity are turned on. Density, current density, and

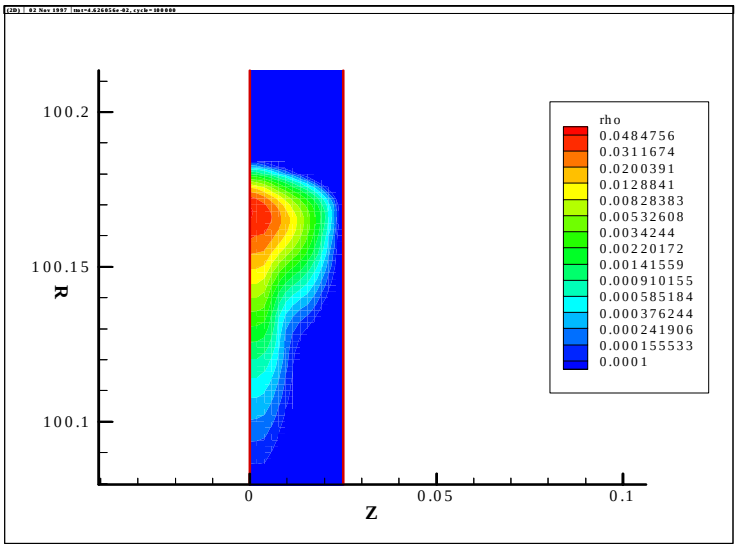

Figure 8-3: Contour plot of ρ (g/cc) at t=.047 μs.

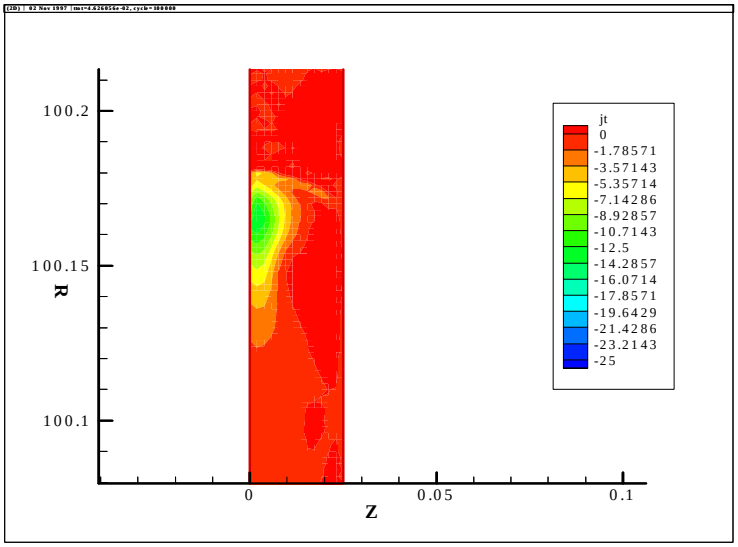

Figure 8-4: Contour plot of j_θ $(10^t A/cm^2)$ at t=.047 μs.

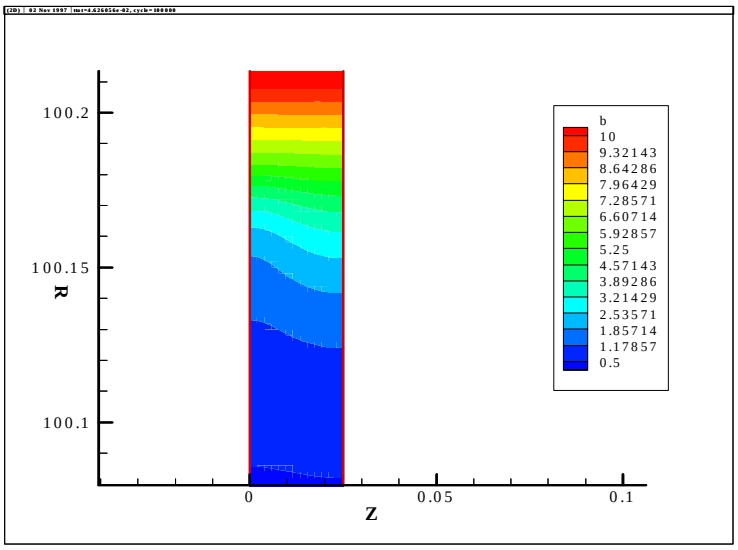

Figure 8-5: Contour plot of rA_θ $(MG \cdot cm)$ at t=.047 μs.

radiation contour plots are shown in figures 8-6 to 8-8.

The density contours show that material is ohmically heated and blown into the gap. Due to magnetic pressure, this low-density material is accelerated towards the axis more rapidly than the "core" of the original wire. However, as more and more material collects between the wires, the magnetic field lines open and more current can flow in this gap region. The current density plots in figure 8-7 show this gap region to eventually carry higher current density than the wire. Accordingly, material is repinched between the gap (figure 8-6). As a final observation, we see radiation temperatures (figure 8-8) of around 20 eV which are consistent with experiment.

Again we see an entirely different set of dynamics than with the single wires in the $r-z$ plane. Because of the connection of magnetic field between the wires, they do not maintain cylindrical symmetry. Material is swept down between the wires, baring the dense core to the magnetic field. This aids in the heating and expansion of the entire wire. Conversely, our 1-D $r-z$ plane results show a low density corona that maintains itself around the wire. We also see material collecting between the wires and forming secondary pinches with

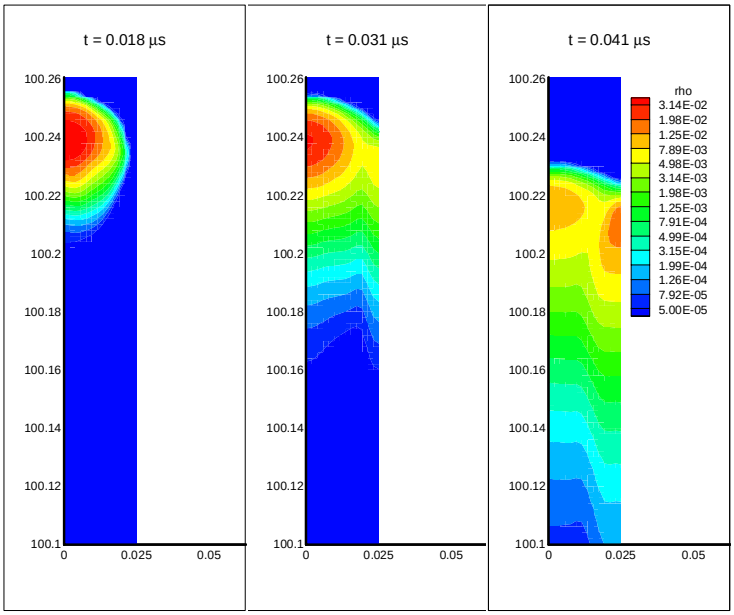

Figure 8-6: Density contour plots for a 10 μm wire in a 180 wire array.

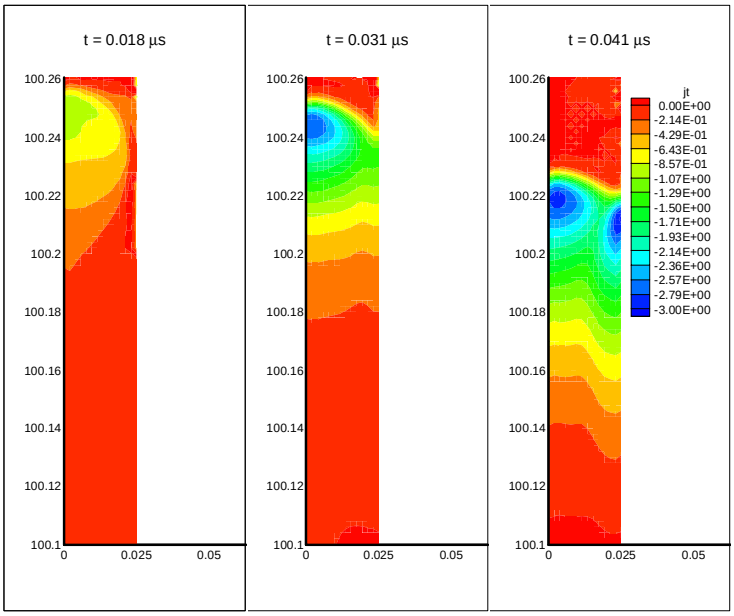

Figure 8-7: Current density contour plots.

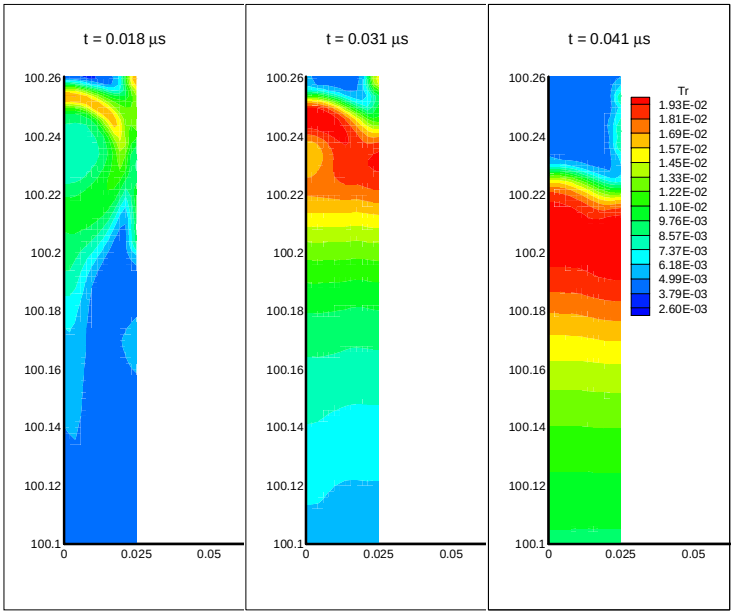

Figure 8-8: Radiation temperature contour plots

current density being "switched" from the original wire.

8.4 120 Wire Array Shots

8.4.1 ALE - Arbitrary Eulerian Lagrangian

We will briefly explain the use of the ALE features of Trac-II in the wire array problem. Up to now, we have described calculations done using pure Eulerian motion in the $R-\theta$ plane. In this mode the grid remains fixed ($\overrightarrow{v}_{grid} = 0$) and the fluid is free to move across zone boundaries. When this occurs, fluid quantities such as mass and energy are advected. One drawback to this method is that numerical "diffusion" occurs as material is advected though the zones. In this case, when the wire moves a distance equal to several wire radii, large energy errors (>10%) begin to appear. Since we wish to eventually follow the wire down to axis, this is unsatisfactory.

The second mode to run Trac-II is pure Lagrangian. In this case the fluid is attached to the zones (nodes) and the mesh in turn moves with the grid velocity ($\overrightarrow{v}_{grid} = \overrightarrow{v}_{fluid}$). This

was the mode used to run the 1-D and 2-D $r-z$ plane calculations. With pure Lagrangian motion, energy errors are typically small ($\sim$ 0.1%). Unfortunately, as mentioned earlier, bowtying mesh distortions cause the runs to terminate prematurely. This fact will prevent this mode from being used in our wire array problems. With low density material being swept rapidly down between the wire gap in the $R-\theta$ plane, the mesh would bowtie before any appreciable wire motion had occurred.

The third mode in which to run Trac-II offers some relief from these problems. It is ALE - Arbitrary Eulerian Lagrangian. In this mode the mesh is moved in a user-defined fashion. First, a Lagrangian step is taken. Then the material is advected according to the relative velocity between grid and fluid:

$$\overrightarrow{v}_{rel} = \overrightarrow{v}_{fluid} - \overrightarrow{v}_{grid}$$

The difficulty is to develop a scheme of assigning $\overrightarrow{v}_{grid}$. In the case of the wire in the $R-\theta$ plane, we chose to move the mesh with the center-of-mass of the wire. In this way, the wire may expand and distort within a set of zones that are in turn rapidly moving radially inward. This minimizes the "crossing" of zones problem while allowing us to follow the overall motion of the wire for a long time. This arrangement is shown in figure 8-9.

In actual problems with ALE it is possible to follow the movement of the wire for up to 1 cm of movement towards axis with small energy errors ($<$ 1%). Since the initial wire array radius is 2 cm, this probably is the limit of our planar approximation. In the future we will extend this ALE method to a wedge geometry. Detailed results of ALE runs will be described in the next section.

8.4.2 Results with 10 and 18 μm Wires

We now revisit our study of the effect of varying initial wire diameter in an array of fixed wire number. We consider 120 wire array shots with two different wire diameters, 10 and 18 μm. As in the previous $R-\theta$ runs we will examine a single wire in a planar array using mirror boundary conditions. The wire will be pre-expanded 10 times and initiated at $t_o = 0.1\ \mu s$.

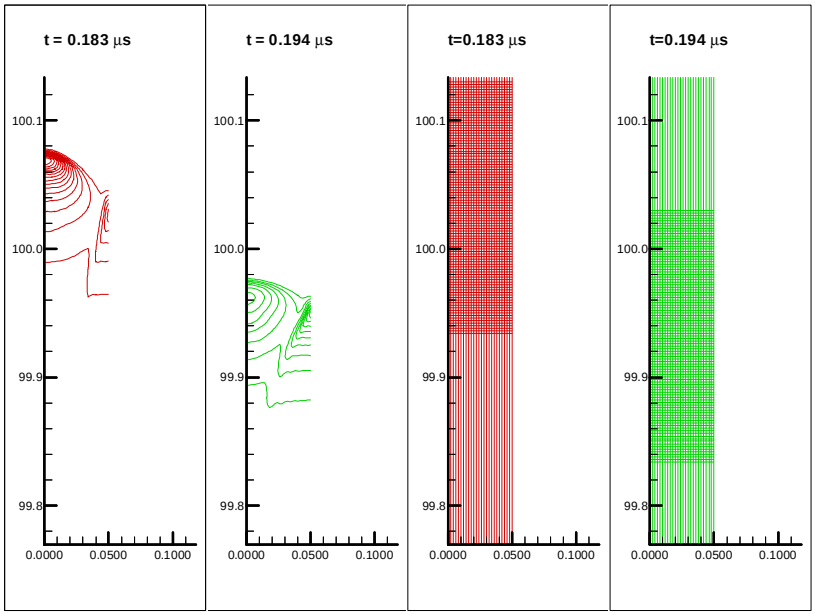

Figure 8-9: ALE run with Trac-II. The mesh moves with the CM velocity of the wire.

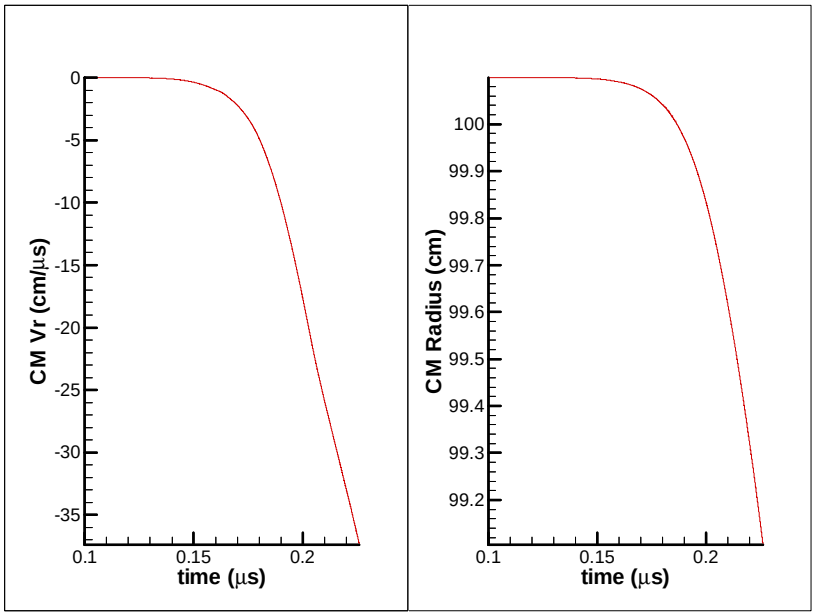

Figure 8-10: CM velocity and position for 18 μm wire.

One obvious difference between the two cases is the width of the current sheath. For the 18 μm wire this is approximately ΔR=1 mm whereas for the 10 μm wire it is smaller - ΔR=1/2 mm. This may be important as the width of the x-ray pulse is governed by the width of the shell that is being accelerated towards the axis. A simple estimate of the pulse width is given by [23]

$$\tau_{\substack{out \\ x-ray}} \approx \frac{\Delta R}{v_{shell}}$$

During this time kinetic energy is converted to thermal energy which is then radiated away. Thus if the difference between shell width persists until convergence, this could explain why the array of 10 μm wires produces a shorter x-ray pulse width than the array of 18 μm wires.

In the case of RT instability growth, the width of the shell is determined by the smearing of mass from the bubble-spike characteristic of the instability [31]. Then the pulse width is given by $\tau_{\substack{out \\ x-ray}} \approx t_{spike} - t_{bubble}$. It is possible that this scale is being determined instead by the initial diameter of the wires and their resulting dynamics. However, more conclusive results would require a $R-\theta$ calculation that is carried out to convergence on axis. These will be performed in the near future.

8.4.3 Hussey-Roderick Density Profile

As mentioned earlier, fluid instabilities become a dominant effect in Z-pinches. 2-D simulations of wire array Z-pinches are carried out in the rz-plane by assuming the wires have merged into a cylindrical shell. An initial perturbation, varying as e^{ikz}, is applied to the plasma shell and the Rayleigh-Taylor instability, which grows as $\gamma = \sqrt{kg}$ in the linear phase, is studied. Through calculations of this type, experiments may be designed which minimize RT growth and thus produce maximum compression and X-ray power.

Generally speaking, the choice of initial shell profile is arbitrary. However, $R-\theta$ runs can provide these initial conditions (i.e. $\rho, T_e, T_i, T_r, B_\phi$ as functions of r) for 2-D rz-plane RT calculations. In figure 8-16 we show the "$\theta - averaged$" density for the 18 μm wire discussed in the previous section. Note that the profile is Gaussian at early times (due to uniform expansion under ohmic heating) but evolves into a shape with a sharp boundary with an exponentially decaying tail.

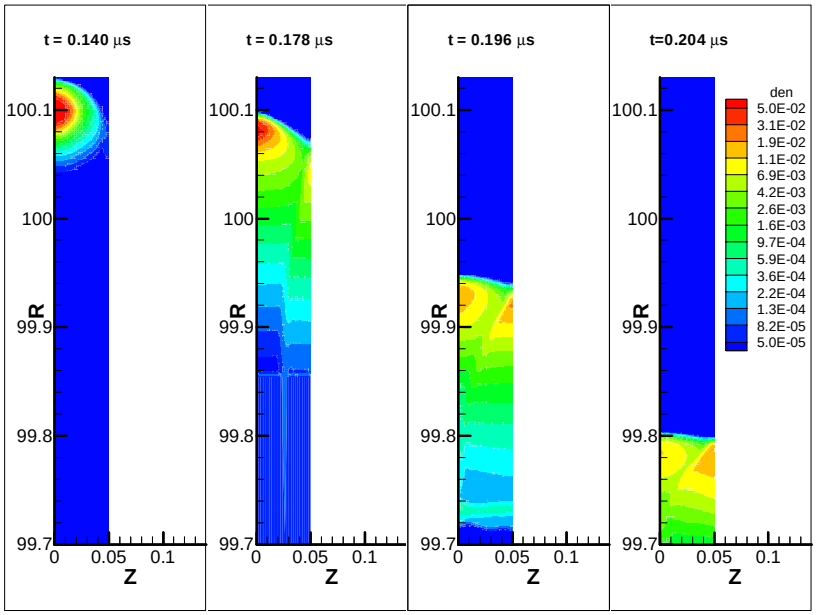

Figure 8-11: Density contours for 18 μm wire.

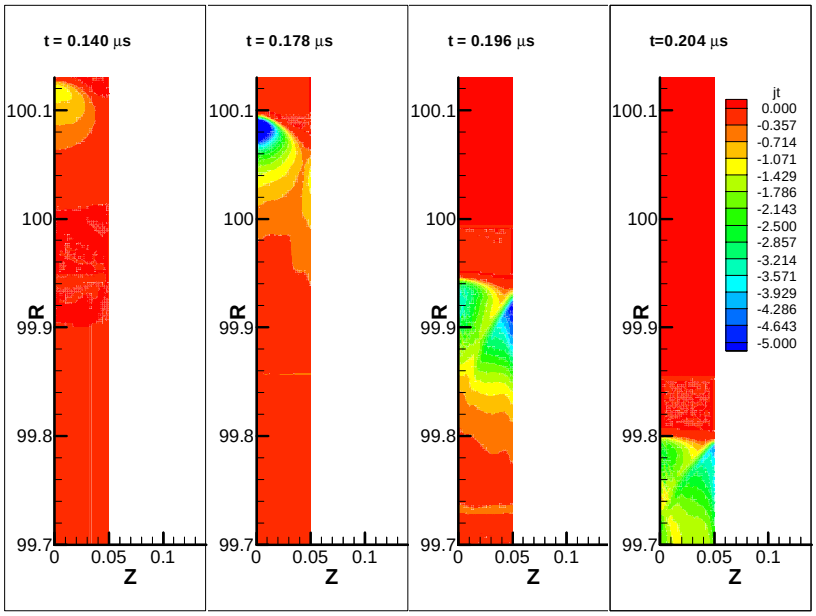

Figure 8-12: Current density contour plots for 18 μm wire.

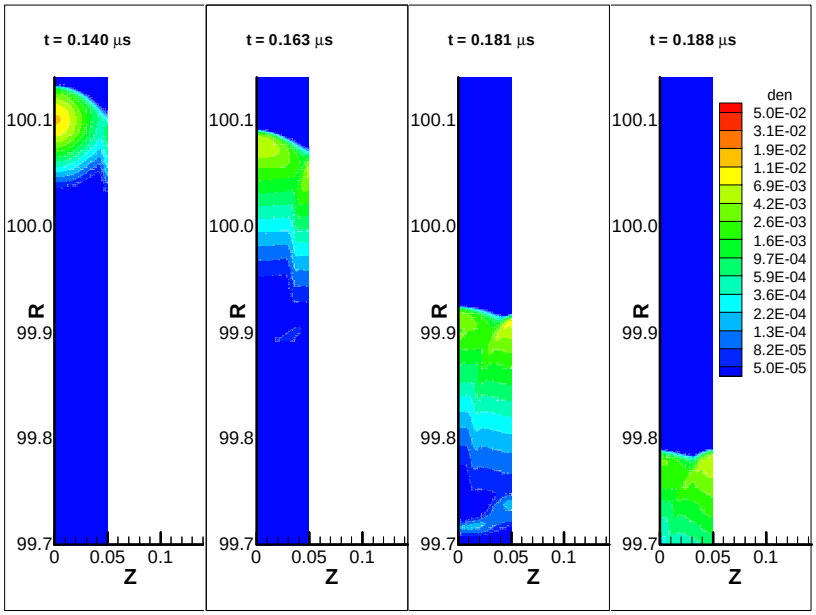

Figure 8-13: Density contours for 10 μm wire.

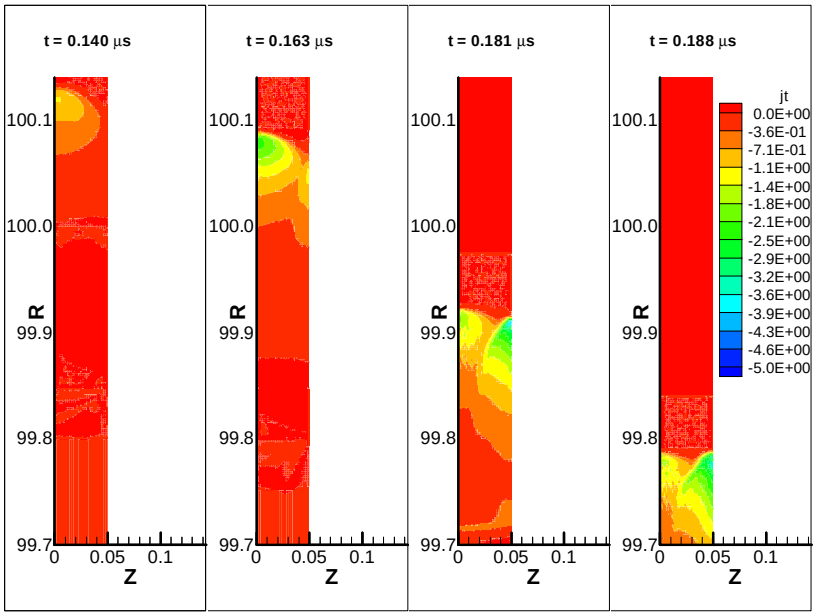

Figure 8-14: Current density contours for 10 μm wire.

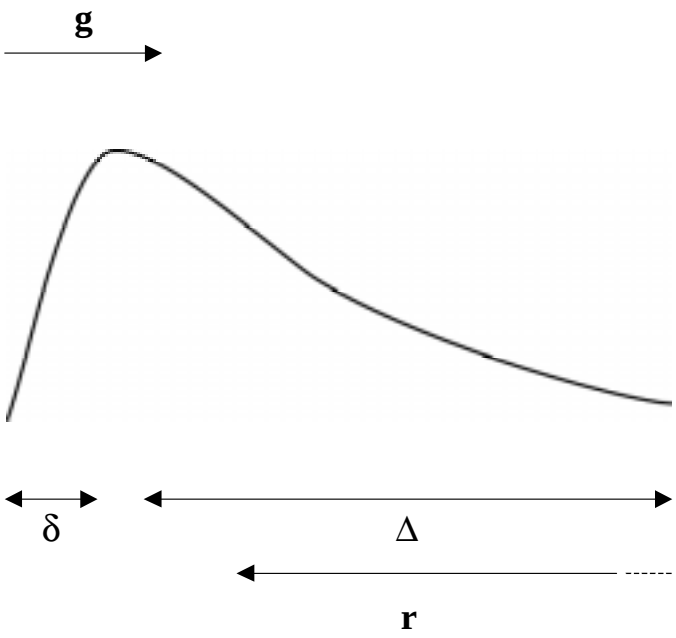

Figure 8-15: Hussey-Roderick density profile.

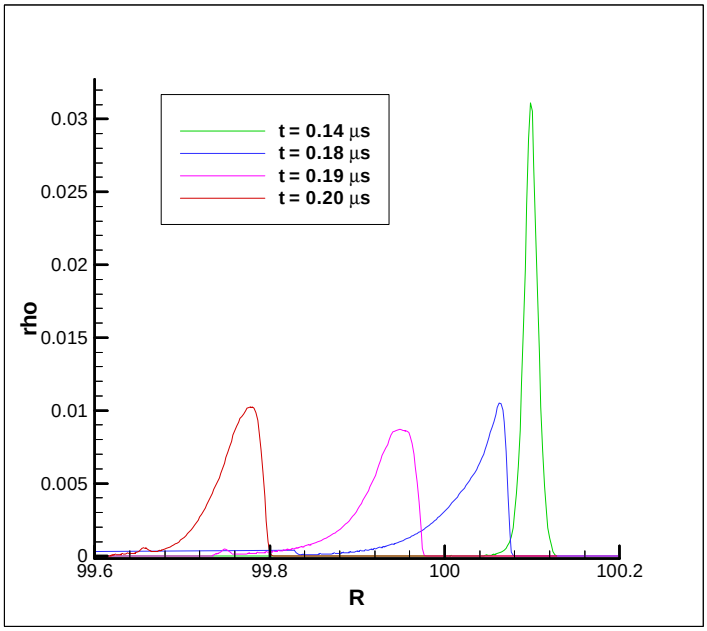

Figure 8-16: θ-averaged density contours for 18 μm wire case.

This profile is commonly seen in r-z plane calculations on cylindrical shells and was calculated analytically by Hussey and Roderick [30][31]. A sketch of this is shown in figure 8-15 It consists of two scales. The first is determined by the resistivity:

$$\Delta = \sqrt{\frac{\eta t}{4\pi}}$$

and the second is determined by the sound speed and acceleration:

$$\delta = \frac{c_s^2}{g}$$

Using force balance we may obtain a simple relation between the two scales

$$\rho \Delta g \approx \frac{B^2}{8\pi}$$

$$\frac{\Delta}{\delta} = \frac{B^2}{8\pi\rho c_s^2} = \frac{P_M}{P} \tag{8.2}$$

where $P_M \equiv \frac{B^2}{8\pi}$ is the magnetic pressure and P is the plasma pressure. For an imploding shell $\frac{P_M}{P} \gg 1$. In the case of the 18 μm wire density profiles shown in figure 8-16 we find rough agreement with equation 8.2 ($\frac{\Delta}{\delta}, \frac{P_M}{P} \approx 10 - 20$).

Chapter 9

TRAC-III

Trac-III is a 3-dimensional resistive MHD code developed by the late Jim Eddleman. All the fluid and magnetic field equations given in Chapter 1 are solved. Trac-III uses tetrahedral elements in a Cartesian (xyz) geometry. Like Trac-II, the magnetic vector potential is treated as a fundamental variable to ensure $\nabla \cdot B = 0$. Presently the code runs only in pure Lagrangian mode but some attempt was made to include Eulerian motion.

For our purposes here we will consider a simple Z-pinch undergoing a kink instability. Similar results were first presented by Jim Eddleman at the 1993 DPP APS meeting. This example will serve to illustrate some of the physics of the Z-pinch while at the same time illustrating the features of Trac-III.

9.1 Derivation of Equilibrium Configuration

We will now derive the equations for the equilibrium configuration of a Z-pinch under specific conditions [1][29]. We begin with our equation of motion (A.2). For the steady state ($\frac{D\overrightarrow{v}}{Dt} = 0$) we have

$$0 = -\nabla (p_e + p_i) + \overrightarrow{J} \times \overrightarrow{B} \tag{9.1}$$

The second term may be rewritten with a vector and Ampere's law:

$$\begin{aligned}\overrightarrow{J}\times\overrightarrow{B} &= -\frac{1}{4\pi}\overrightarrow{B}\times\left(\nabla\times\overrightarrow{B}\right)\\ &= -\nabla\left(\frac{B^2}{8\pi}\right)+\frac{1}{4\pi}\overrightarrow{B}\cdot\nabla\overrightarrow{B}\end{aligned}\tag{9.2}$$

The first term in equation 9.2 is referred to as the magnetic pressure term with $p_M \equiv \frac{B^2}{8\pi}$ and the second term is called the magnetic tension term. In our case the second term vanishes as $\overrightarrow{B} = B_\phi(r)\,\widehat{\phi}$. Writing $p = p_e + p_i$ we have

$$\begin{aligned}0 &= -\nabla p - \nabla\left(\frac{B^2}{8\pi}\right)\\ &= -\frac{\partial p}{\partial r} - \frac{B_\phi}{4\pi r}\frac{\partial}{\partial r}\left(rB_\phi\right)\end{aligned}\tag{9.3}$$

Integrating over r we obtain

$$\begin{aligned}\int\frac{\partial p}{\partial r}dr &= -\int\frac{B_\phi}{4\pi r}\frac{\partial}{\partial r}\left(rB_\phi\right)dr\\ p(r) &= p_o - \int_0^r\frac{B_\phi}{8\pi r^2}\frac{\partial}{\partial r}\left(r^2B_\phi^2\right)dr\end{aligned}\tag{9.4}$$

Since our cylindrical plasma extends to $r = r_o$ we have $p(r_o) = 0$ and we may write

$$p_o = \int_0^{r_o}\frac{B_\phi}{8\pi r^2}\frac{\partial}{\partial r}\left(r^2B_\phi^2\right)dr\tag{9.5}$$

combining this with equation 9.4 we obtain our pressure profile equation

$$p(r) = \int_r^{r_o}\frac{B_\phi}{8\pi r^2}\frac{\partial}{\partial r}\left(r^2B_\phi^2\right)dr\tag{9.6}$$

Next we solve our pressure equation for a specific configuration. If we assume that J_z, our current density, is constant throughout the plasma ($r < r_o$) and zero outside the plasma

we obtain, by Ampere's law,

$$\begin{aligned} B_\phi &= \frac{2rI}{r_o^2} \ (r < r_o) \\ &= \frac{2I}{r} \ (r > r_o) \end{aligned} \tag{9.7}$$

Substituting equation 9.7 into equation 9.6 and integrating over r we obtain a parabolic pressure profile for this constant current density case.

$$p\left(r\right) = \frac{I^2}{\pi r_o^2}\left(1 - \frac{r^2}{r_o^2}\right) \tag{9.8}$$

9.2 Kink Instability

As discussed in Chapter 5 an axially symmetric perturbation of Bennett Equilibrium will produce sausage modes which grow exponentially. Similarly, if the plasma column is perturbed as a kink, this instability will grow as well. The reason behind this is that magnetic field lines (B_ϕ) on the concave side will be closer together than on the convex side. Thus the magnetic pressure on the convex side is higher than on the concave side. This will in turn cause the perturbation to grow. The growth rate for this mode is given by [4]

$$\gamma^2 = \frac{B_\phi^2 k^2}{4\pi\rho} \ln\left(\frac{kr_o}{2}\right)$$

for long wavelength ($\lambda \gg R$) and assuming an ideal plasma with no magnetic field enclosed inside the Z-pinch (Bennett Equilibrium). Usually we may make a simple estimate of the growth rate with

$$\gamma \sim v_A k$$

where $v_A = \sqrt{B^2/4\pi\rho}$ is the Alfvén velocity.

9.3 Computational Setup

A Z-pinch is initialized with a parabolic density profile. The boundaries are ideal conductors and a slip velocity condition is applied to either end of the pinch. The current, magnetic

field, and pressure are given by

Variable	$r < r_o$	$r > r_o$
j_z	$\frac{I_o^2}{\pi r_o^2}$	0
B_ϕ	$\frac{2rI_o}{r_o^2}$	$\frac{2I_o}{r}$
p	$\frac{I_o^2}{\pi r_o^2}\left(\frac{1}{1-\varepsilon} - \frac{r^2}{r_o^2}\right)$	$\frac{\varepsilon I_o^2}{\pi r_o^2}$

In this specific case $I_o = 10$ MA, $r_o = 2\ mm$, $T_e = T_i = 100\ eV$, and $\varepsilon = \frac{1}{25}$. The density and energy will be generated using the pressure profile condition and the Ideal Gas Law ($\overline{Z} = \overline{A} = 1$).

The kink will be seeded with a helical velocity perturbation given by

$$\begin{aligned} v_z &= v_o \cos(\theta) \\ v_y &= v_o \sin(\theta) \\ \theta &= kx - \phi \end{aligned}$$

In this example $\theta = \pi\left(\frac{x}{2} - 1\right)$ and $v_o = 1\ cm/\mu s$. The velocity will be applied along the center line of the pinch. The growth rate can be estimated by $\gamma \sim v_A k = 25\ 1/\mu s$.

The initial velocity field and pressure contour plots are shown in figures 9-1 and 9-2. We will enclose our Z-pinch in a box of length equal to the perturbation wavelength, $L_x = \lambda = 4$ cm. The width and height (L_x, L_y) will be equal to 1 cm.

9.4 Kink Mode Results

In figures 9-3 through 9-6 we show the growth of the kink mode in the wire. The wire undergoes $\gamma t \approx 9$ e-foldings during its 0.37 μs run. During this time it grows nonlinearly, seeking a shorter wavelength. This final wavelength is $\lambda = 1.6\ cm$ and is probably determined by the resolution of our mesh (12,000 tetrahedral zones constructed from a $10 \times 10 \times 10$ hexagonal zones). The pinch is stabilized by the proximity of the walls as well as rotated towards its corners.

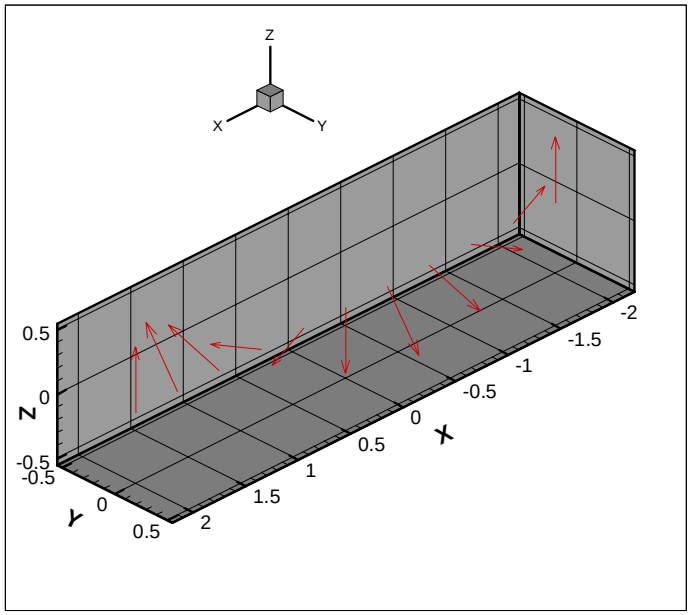

Figure 9-1: Initial velocity for kink mode

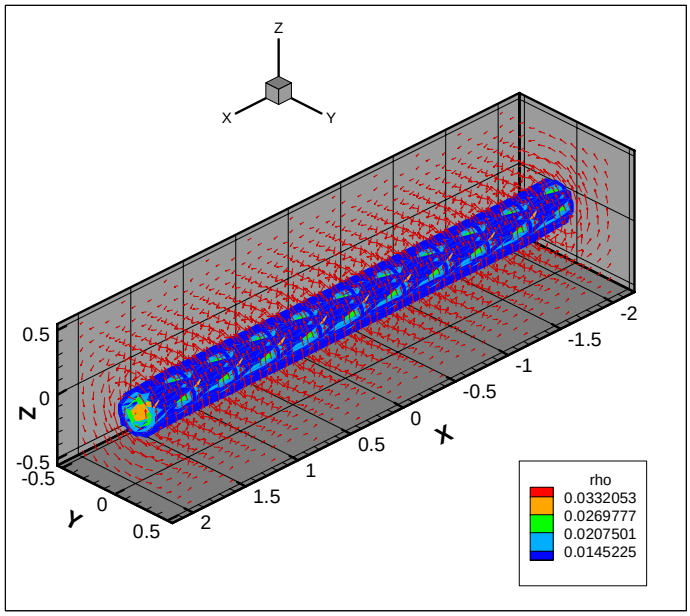

Figure 9-2: Initial pressure contour plot for Z-pinch

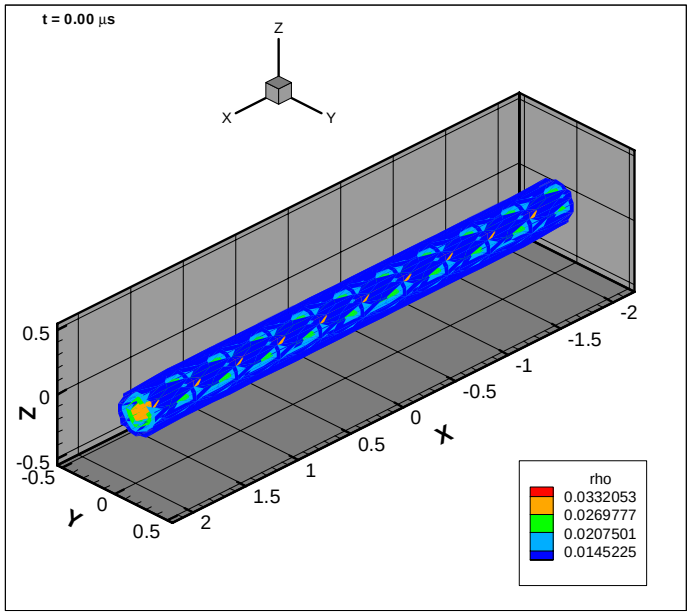

Figure 9-3:

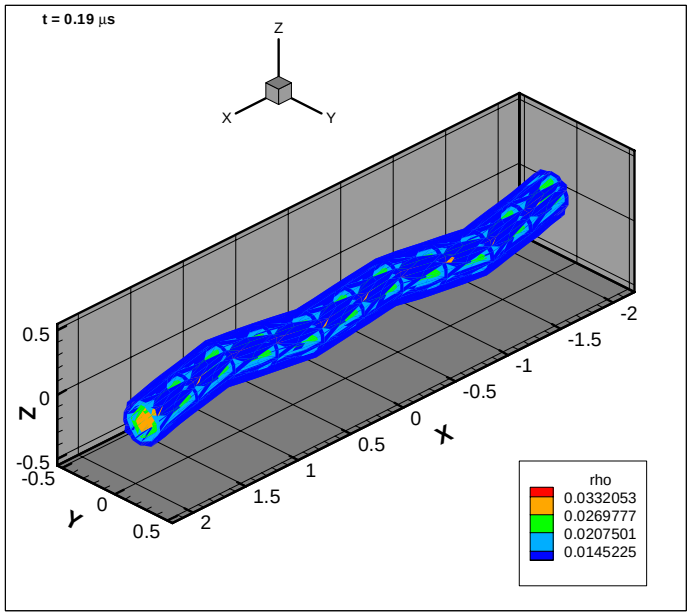

Figure 9-4:

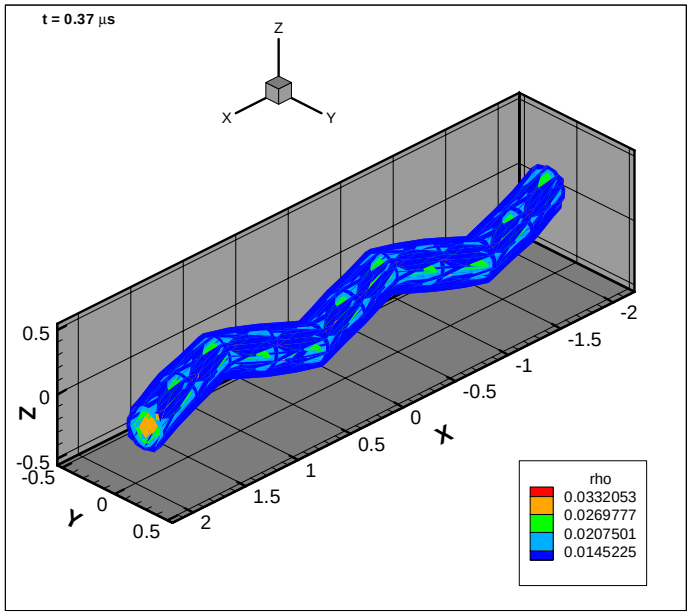

Figure 9-5:

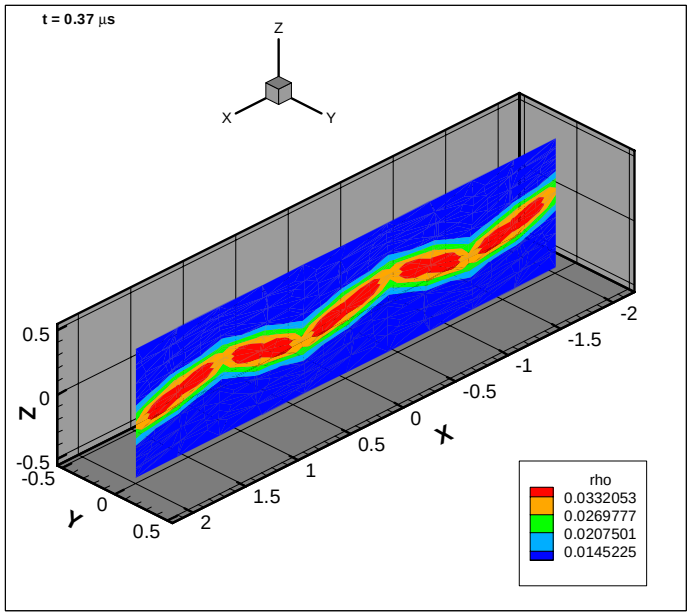

Figure 9-6: Density slice plot.

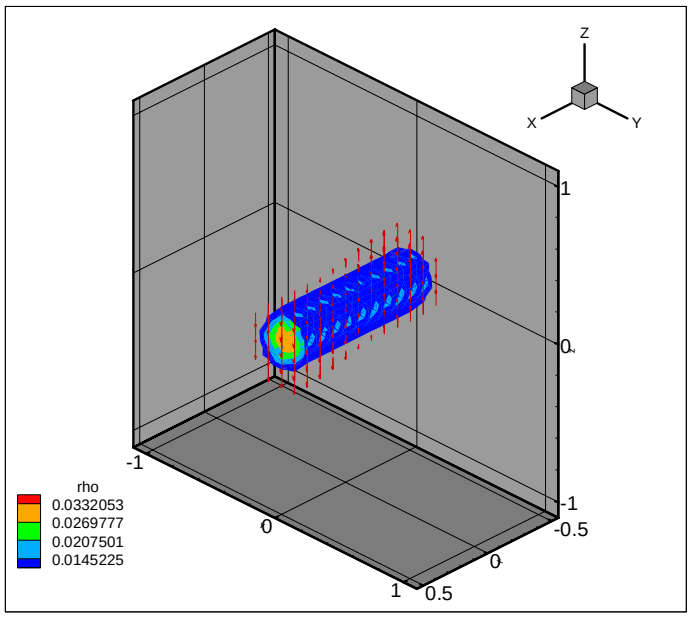

Figure 9-7: Pressure and velocity distribution for Z-pinch.

9.5 Additional Calculations

Next we consider a slightly different arrangement. We use the exact same pressure profile but the computational box is only a half wavelength long. To reduce the effects of the walls in stabilizing, as well as rotating, the plasma column the walls are moved out farther. Our Z-pinch will now be contained in a $1 \times 2 \times 2$ cm computational box. We will perturb our Z-pinch in the xz plane with the following cosine velocity distribution

$$v_z(r) = v_o \cos(kx + \phi) \quad \text{for } r < r_o$$

In this case we will take $k = \pi$ ($\lambda = 2$ cm) and $\phi = \dfrac{\pi}{2}$. The arrangement is shown in figure 9-7.

To monitor the growth of the kink mode we will examine the kinetic energy. Its growth will be given by

$$KE \sim \exp(2\gamma t)$$

before nonlinear effects arise. Thus a log plot of the kinetic energy will reveal the growth

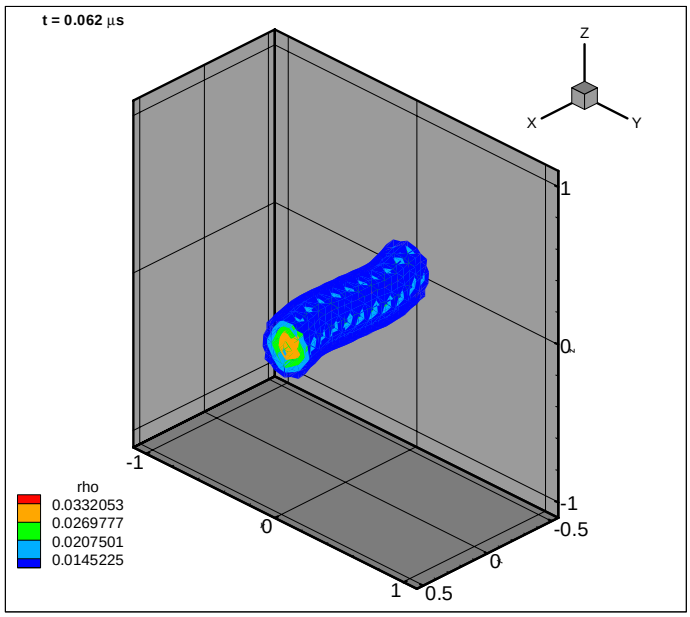

Figure 9-8:

rate.

Contour plots of density are shown in figures 9-8 through 9-11. Again we see that the ends of the Z-pinch are attracted towards the corners and the entire column is rotated buy a 45^o angle.

We may roughly estimate the growth rate through the Alfvén speed. Using the largest density contour ($\rho = 0.033\ g/cc$) and the magnetic field just outside the plasma ($B_\phi = 10\ MG$) we find that $\gamma = v_A k = 49\ 1/\mu s$. Using the plot of log(KE) ($\sim 2\gamma t$) vs. time in figure 9-12 we find a growth rate of $\gamma \approx 45\ 1/\mu s$. Even with this crude estimate we see that Trac-III is in fairly good agreement with the analytic theory.

9.6 The Wire Array Z-Pinch

Jim Hammer and Dimitri Ryutov have recently derived analytic growth rates in the linear regime for the case of a planar array of wires [32]. This type of configuration was modeled with 2-D $R-\theta$ plane calculations in chapter 8. The instability growth can be separated into two modes - a transverse mode and the traditional RT mode. Although our "box" geometry

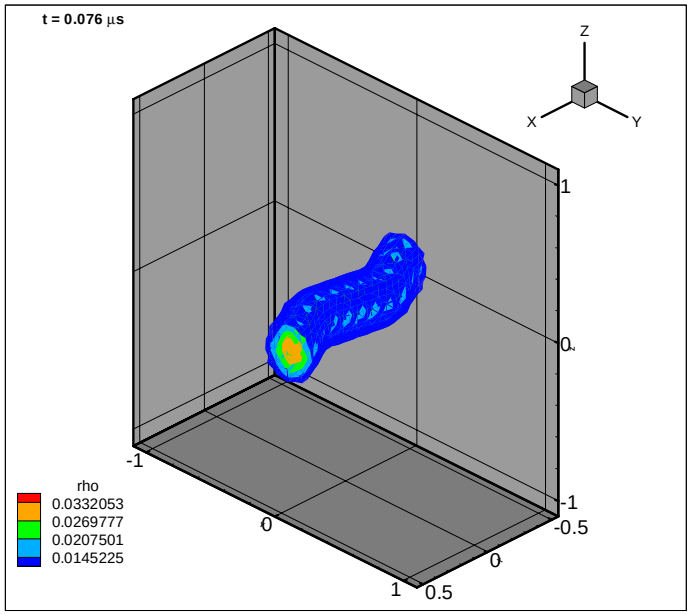

Figure 9-9:

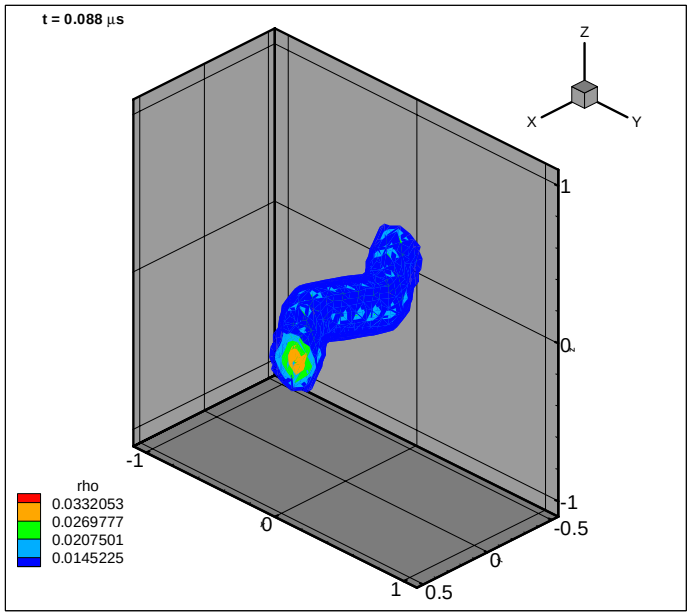

Figure 9-10:

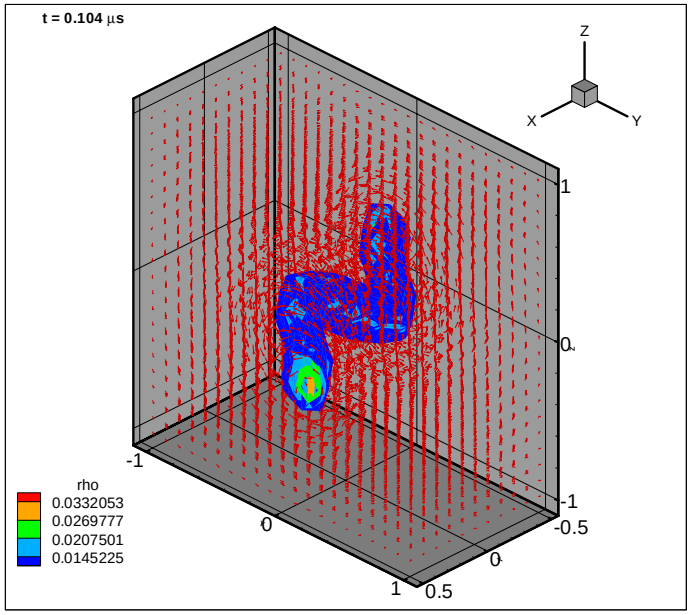

Figure 9-11: Density contour and magnetic field plot.

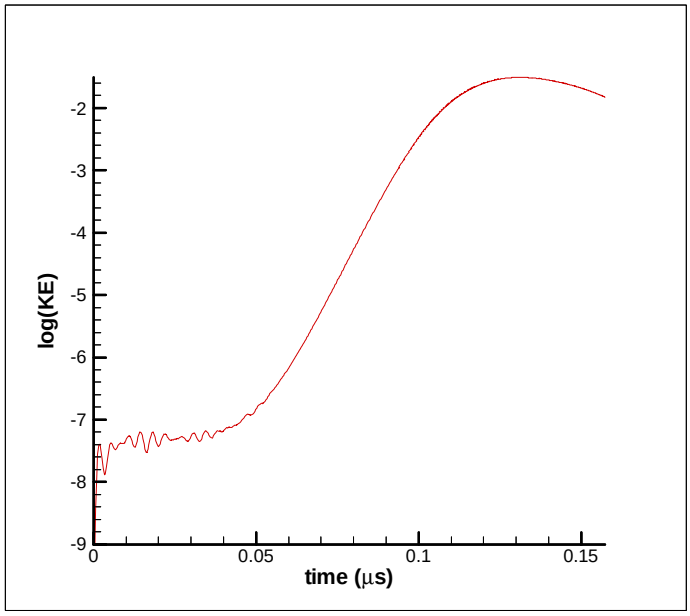

Figure 9-12: Plot of ln(KE) vs. time for 3-D z-pinch.

produced some annoying effects when trying to model a simple Z-pinch (i.e. rotation towards the diagonal) , it is ideally suited for the planar 3-D array problem. With the addition of mirror boundary conditions at either end of the box, a single wire or multiple wires in a planar array may be studied. In the future, calculations of this type will be performed and compared to the analytic theory. Having established agreement with theory, the full problem - the 3D wire array in the PBFA-Z experiment - will be treated.

Chapter 10

Summary and Conclusions

This thesis describes a study of various aspects of Z-pinches with Trac-II and Trac-III. First, modifications were made to Trac-II to allow modeling of dense high Z materials like those used in the wire array Z-pinch experiments. This included adding radiation diffusion, a 4-phase EOS and conductivity model, and a new implicit poloidal field solver. Then, using the PBFA-Z circuit parameters, the wire array Z-pinch at the Z accelerator at SNL was studied. In chapter 5 the behavior of a single wire in the array was examined. In chapter 6 we looked at the growth of the "sausage" instability in single wires. Calculations in the $R-\theta$ plane, the cross sectional view of the wire, were performed in chapter 8. This demonstrated the dynamics of the wire as it is influenced by neighboring wires while being accelerated towards the axis. In chapter 9 Trac-III, a 3-D MHD code was introduced and used to illustrate the "kink" instability.

Several conclusions may be drawn from this study:

1. The wire remains solid well into the current pulse and has a core-corona structure. Radiation flow that occurs during repinching of the corona is responsible for melting the wire.

2. During the expansion phase of the wire, there is little sausage instability growth.

3. For the case of the 120 wire array at fixed radius, sausage growth does not vary appreciably with initial wire radius.

4. 1-D runs indicate that, consistent with experiment, the 1 mm gap length is an important scale. In the 120 wire case, the plasma expands to just about half the gap distance. This indicates that repinching, and thus a growth of the sausage mode, could occur.

5. 2-D $R-\theta$ plane calculations show that the current sheath of the small diameter wires is narrower than that of the large diameter wires. Since pulse width scales as sheath width, this could possibly explain why arrays with a smaller initial wire radius have a narrower x-ray pulse width.

6. 2-D $R-\theta$ plane simulations show that the wires do not remain as well-defined individual Z-pinches that are being accelerated towards the axis. However, even though the Hussey Roderick profile is reproduced, they do not form a uniform plasma shell as assumed in 2-D RT calculations.

7. To most accurately and conclusively study the growth of instabilities in the wire array Z-pinch, 3-D calculations are necessary. The question of whether individual wire behavior (i.e. merging and sausage modes) or "shell" behavior (RT modes) are the determining factor in Z-pinch performance could be resolved.

10.1 Future Tasks

As noted in the previous chapters, several modifications are needed in the Trac-II and Trac-III codes. These include:

1. Conversion of "splitting" routines into fully implicit routines solved with ICCG. This will greatly reduce the noise seen in 2-D perturbation problems

2. Inclusion of "wedge" geometry in the $R-\theta$ plane. This combined with the ALE method described in chapter 8 should allow runs to be carried out until convergence on axis.

3. Updating Trac-III to include many of the physics routines already in Trac-II. These include radiation diffusion, QEOS, and 4-phase conductivity.

In addition to these changes, several studies are planned with Trac-II and Trac-III in the near future:

1. The critical current problem (described in Chapter 4) will be examined using the 2-D geometry of the PBFA-Z apparatus.

2. A study of RT growth in the 2D $R-\theta$ plane will be performed using a test particle under the influence of the velocity field from a wire array run. If material (the test particle) is being carried away from regions where $\frac{\partial \rho}{\partial r} < 0$, this will reduce the growth of the RT mode which is given by $\gamma = \sqrt{g \frac{1}{\rho} \frac{\partial \rho}{\partial r}}$.

3. Trac-II will be benchmarked with single wire experiments soon to be performed at the Nevada Terawatt Facility. These experiments will provide detailed density profiles along with information such as expansion velocity and the amount of material participating in the corona. Comparison of Trac-II with this type of data would help in validating the EOS and conductivity models used in the code.

4. Using Trac-III, transverse and RT modes that develop in planar arrays of wires will be studied. Initially the ideal case in the linear regime will be considered and compared to theory. Then, with Trac-III updated with the physics packages used to model dense plasmas, a study of the actual PBFA-Z wire array Z-pinch may be performed.

Appendix A

Introduction to TRAC-II

Trac-II is a two dimensional axisymmetric resistive magnetohydrodynamic code developed by the late Jim Eddleman. It simulates all three spatial components (r, z, and azimuthal) of the magnetic field and fluid velocity vectors, and the plasma is treated as a single fluid with two temperatures (electron and ion). In addition, it can optionally include a self-consistent external circuit to model capacitor bank energy sources. Recent modifications of the code include the addition of a 3-T radiation model, a 4-phase equation of state and conductivity model, and an implicit solver for poloidal (B_z, B_r) magnetic field diffusion. These changes allow the detailed study of fiber and wire array Z-pinches for high Z materials.

A.1 Equations Solved in Trac-II

Continuity Equation

$$\frac{\partial \rho}{\partial t} + \nabla \cdot (\rho \overrightarrow{u}) = 0 \tag{A.1}$$

Momentum Equation

$$\frac{\partial (\rho \overrightarrow{u})}{\partial t} + \nabla \cdot (\rho \overrightarrow{u}\,\overrightarrow{u}) = -\nabla (P_e + P_i) + \left(\overrightarrow{J} \times \overrightarrow{B} \right) + \nabla \cdot \overline{\overline{Q}} \tag{A.2}$$

Electron-Energy Equation

$$\frac{\partial(\rho\varepsilon_e)}{\partial t} = -P_e\nabla\cdot\overrightarrow{u} + \eta J^2 - P_{rad} + \nabla\cdot(\overline{\overline{K}}_e\cdot\nabla T_e) + \alpha_{ei}(T_i - T_e) \tag{A.3}$$

Ion Energy Equation

$$\frac{\partial(\rho\varepsilon_i)}{\partial t} = -P_i\nabla\cdot\overrightarrow{u} + \overrightarrow{u}\cdot\nabla\cdot\overline{\overline{Q}} + \nabla\cdot(\overline{\overline{K}}_i\cdot\nabla T_i) + \alpha_{ei}(T_e - T_i) \tag{A.4}$$

Faraday's Law

$$\frac{\partial\overrightarrow{B}}{\partial t} = -\nabla\times\overrightarrow{E} \tag{A.5}$$

Ohm's Law

$$\overrightarrow{E} = \eta\overrightarrow{J} - \overrightarrow{u}\times\overrightarrow{B} \tag{A.6}$$

Ampere's Law

$$\overrightarrow{J} = \frac{1}{4\pi}\nabla\times\overrightarrow{B} \tag{A.7}$$

A.2 Additions to Trac-II

We briefly summarize the modifications made to Trac-II:

A.2.1 The 3-T Radiation Diffusion Model.

The "3-T" model is a single group model for radiation that is given by [8]

$$\frac{\partial(aT_r^4)}{\partial t} = -\nabla\cdot\overrightarrow{F_l} + P_r\nabla\cdot\overrightarrow{u} + \nabla\cdot\left(\overrightarrow{u}aT_r^4\right) + ac\rho\kappa_P\left(T_e^4 - T_r^4\right)$$

where the flux is given by

$$\overrightarrow{F_l} = -\frac{\frac{c}{3}\nabla\left(aT_r^4\right)}{\rho\kappa_R + \frac{2\left|\nabla T_r^4\right|}{3T_r^4}}$$

and the radiation pressure is defined as

$$P_r \equiv \frac{1}{3}aT_r^4$$

The model assumes optically thick material but is flux limited in free-streaming limit:

$$\frac{c}{3\rho\kappa_R}\left|\nabla\left(aT_r^4\right)\right| \gg \frac{ca}{2}T_r^4$$

$$\left|\overrightarrow{F_l}\right| \rightarrow -\frac{ca}{2}T_r^4$$

The diffusion part of the model is solved implicitly with Incomplete Cholesky Conjugate Gradient (ICCG).The Planck and Rosseland opacities (κ_P and κ_R, respectively) are provided through tables from the super transition array (STA) model [35][24].

A.2.2 Solid-Liquid-Vapor Conductivity Model

For the solid and liquid phases, a simple conductivity is calculated. This is based on the Mott-Jones model implemented in CALE [22]. Melt and boil temperatures from Lindemann's law are calculated to decide which phase is appropriate. The vapor conductivity ($\frac{1}{\sigma_v} = \eta_v = \eta_{ei} + \eta_{en}$) is calculated using the ideal gas Saha equation.

Thermal conductivity in these three phases is calculated from the Wiedemann-Franz law which relates thermal to electrical conductivity:

$$\frac{K}{\sigma} = \frac{\pi^2}{3}\left(\frac{k_B}{e}\right)^2 T$$

A.2.3 Lee-More Conductivity

Solving the Boltzmann equation with the Fermi-Dirac electron distribution, the transport coefficients $\sigma_\perp$ and $K_\perp$ (electrical and thermal conductivity) are calculated (in tabular form) as functions of $(\mu/T_e, \omega_e\tau)$.μ is the chemical potential, ω_e is the cyclotron frequency, and τ is the electron relaxation time [10].

A.2.4 Quotidian Equation of State (QEOS)

QEOS is a self consistent analytic model which is valid over a large range of densities and temperatures [11]. The electron part of the EOS uses Thomas Fermi electron equation of

state. Using the free energy (in tabular form) the quantities

$$\varepsilon_i, c_{vi}, P_i, Z^*, \mu$$

are calculated as functions of $\left(\rho, T_e, \overline{Z}, \overline{A}\right)$. Z^* is the charge state of the atom. $\overline{Z}$ and $\overline{A}$ are the atomic number and atomic mass, respectively.

For the ion part of the EOS, the Cowan Ion Model is used. The quantities

$$\varepsilon_i, c_{vi}, P_i$$

are calculated as functions of $\left(\rho, T_i, \overline{Z}, \overline{A}\right)$.

QEOS also incorporates an empirical bonding model which requires various bonding parameters such as uncorrected pressure and energy, solid density, and the difference between uncorrected and corrected bulk modulus.

A.2.5 Implicit Solution of Poloidal Magnetic Field Diffusion

The Poloidal magnetic field $\overrightarrow{B_p} = (B_z, B_r)$ diffusion was previously calculated explicitly. The implicit solution is a 9-point scheme based on the vector potential A_θ. It is derived using Eddleman's definitions for magnetic field:

$$\overrightarrow{B}_p = -\frac{1}{\Delta V_{zone}} \oint_{boundary}^{zone} (rA_\theta)\, \overrightarrow{dl}$$

(which follows from integrating $\overrightarrow{B} = \nabla \times \overrightarrow{A}$ around the zone volume), Ampere's law and Faraday's law:

$$\frac{\partial}{\partial t}(rA_\theta) = -r \langle \eta \rangle J_\theta$$

The resulting matrix is solved with ICCG. The implicit solution of poloidal magnetic field allows modeling of problems with large vacuum regions (i.e. the cross section of a single wire in a wire-array Z-pinch) as well as stability for large time steps.

Bibliography

[1] T.J.M. Boyd and J.J. Sanderson, Plasma Dynamics, Barnes & Noble, Inc., New York, 1969.

[2] P.A. Sturrock, Plasma Physics, Cambridge University Press, Cambridge, England, 1994.

[3] N.A. Krall and A.W. Trivelpiece, Principles of Plasma Physics, San Francisco Press, Inc., San Francisco, CA, 1986.

[4] J.A. Wesson, "Plasma Stability Theory", Plasma Physics: Lectures from the Culham Plasma Physics Summer School, The Institute of Physics, London, England, 1974.

[5] A. Munier and R. Weaver, Computer Physics Reports, Vol, 3, 169 (1986).

[6] J.R. Buchler, J. Quant. Spectrosc. Radiat. Transfer , Vol. 22, 293 (1979).

[7] J.R. Buchler, J. Quant. Spectrosc. Radiat. Transfer , Vol. 30, 395 (1979).

[8] D. Mihalas and B.W. Mihalas, Foundations of Radiation Hydrodynamics, Oxford University Press, Oxford, England, 1984.

[9] W.H. Press, S.A. Teukolsky, W.T. Vetterolsky, and B.P. Flannery, Numerical Recipies in C, Cambridge University Press, Cambridge, England, 1992.

[10] Y.T. Lee and R.M. More, Phys. Fluids 27, 1273 (1984).

[11] R.M. More, K.H. Warren, D.A. Young, and G.B. Zimmerman, Phys. Fluids 31, 3059 (1988).

[12] N.F. Mott and H. Jones, Theory of the Properties of Metals and Alloys, Oxford U.P., Oxford, England, 1936.

[13] C. Kittel, Introduction to Solid State Physics, John Wiley & Sons, Inc., New York, 1986

[14] N.W. Ashcroft and N.D. Mermin, Solid State Physics, W.B. Saunders Company, 1976.

[15] CRC Handbook of Chemistry and Physics, CRC Press, Inc., Boca Raton, FL, E-64-65 (1982).

[16] Melissa Douglas, Ph.D. thesis, University of New Mexico (1994).

[17] T.W.L. Sanford et. al., Phys. Rev. Lett. 77, 5063 (1996).

[18] T.W.L. Sanford et. al., "Wire Number Doubling in Plasma-Shell Regime Increases Z-Accelerator X-Ray Power", SAND97-2688, Nov. 1997.

[19] W.A. Stygar and R.B. Spielman, "Calculations of Energy Loss to Conductors at High Current Densities", SNL memo, July 1998.

[20] Daniel Kalantar, Ph.D thesis, Cornell University (1993).

[21] A. Mingaleev, S. Pikuz, T. Shelkovenko, and D. Hammer, "Studies of High Density Exploding-Wire-Plasma Structure in Detail Using High Resolution X-ray Backlighting", LPS Report #98-02, Laboratory of Plasma Studies, Cornell University (1998).

[22] CALE user's manual and generator.

[23] Jim Hammer, Lawrence Livermore National Laboratory, Livermore, CA, private communication.

[24] Brian Wilson, Lawrence Livermore National Laboratory, Livermore, CA, private communication.

[25] P. Brown, E. Chow, and Y. Saad, "ICT - A Dual Threshold Incomplete LDL^T factorization", LLNL UCRL Technical Report, in preparation.

[26] Statistical Physics, L.D. Landau and E.M. Lifshitz, Pergamon Press, Oxford, England, 1958.

[27] B. Ya. Zel'dovich and Yu. P. Raizer, Physics of Shock Waves and High Temperature Hydrodynamic Phenomena, Academic, New York, 1966.

[28] G.B. Zimmerman and R.M. More, QEOS subroutines, Lawrence Livermore National Laboratory, Livermore, CA (1984).

[29] J.D. Jackson, Classical Electrodynamics, John Wiley & Sons, Inc., New York, 1975.

[30] T.W. Hussey and N.F. Roderick, Phys. Fluids 24, 1384 (1981).

[31] J.H. Hammer et al, Phys. Plasmas 3, 2063 (1996).

[32] J.H. Hammer and D. Ryutov, "Linear Stability of an Imploding Wire Array", in preparation.

[33] J.A. Harte, et. al., "LASNEX - A 2-D Physics Code for Modeling ICF", UCRL-LR-105821-96-4, ICF Quarterly Report No. 4, Vol. 6, 150 (1996).

[34] "Highlights of the Pulsed Power Inertial Confinement Fusion Program", SNL, Feb. 1998.

[35] A. Bar-Shalom, J. Oreg, W.H. Goldstein, D. Shvarts, and A Zigler, Phys. Rev. A 40, 3183 (1989)